Elsevier Editorial System(tm) for Journal of Alloys and Compounds

Manuscript Draft

Manuscript Number: JALCOM-D-19-10924R1

Title: Thermodynamics of the iron-nitrogen system with vacancies. From first principles to applications

Article Type: Full Length Article

Keywords: A. metals and alloys
B. solid state reactions
C. atomic scale structure
C. phase transitions
C. point defects
D. thermodynamic modelling

Corresponding Author: Dr. Michael Auinger,

Corresponding Author's Institution: University of Warwick

First Author: Aurash Karimi

Order of Authors: Aurash Karimi; Michael Auinger

Abstract: Density Functional Theory (DFT) and Atomistic Kinetic Monte Carlo is employed in this work to assess the thermodynamic behaviour of the α (BCC) and γ (FCC) allotropes in the iron-nitrogen system. The calculated nitrogen solubility at unit nitrogen activity from (250 < T < 1538°C) is found to be significantly underestimated, beyond the uncertainty range of the calculation, in both phases. The boundary of the α-γ phase change as featured in Lehrer diagrams is calculated within the nitriding potential (0.001 < r_N < 10) and temperature (300 < T < 900°C) ranges. The boundary shows good agreement with experimental data, but the calculated α region is consistently smaller than the data suggests. Motivated by the existence of grain boundaries and other common defects which cause far more unoccupied volume within iron than is expected in idealised lattice structures, the effect of excess vacancy concentrations in varying ranges between 10^{-12} < c_v < 10 at.% on nitrogen solubility and the α-γ phase change is quantified. It is shown how discrepancies between the theoretical ideal crystal and experimental data can be "corrected" by excess vacancies to model the non-ideality of iron lattices in reality, and evidence is given for the validity of this correction.
Results are presented in an applied context, allowing opportunities for experimental verification.

Thermodynamics of the iron-nitrogen system with vacancies. From first principles to applications

Aurash Karimi[a,*], Michael AUINGER[a,*]

[a]*WMG, University of Warwick, Coventry CV4 7AL, United Kingdom*

Abstract

Density Functional Theory (DFT) and Atomistic Kinetic Monte Carlo is employed in this work to assess the thermodynamic behaviour of the α (BCC) and γ (FCC) allotropes in the iron-nitrogen system. The calculated nitrogen solubility at unit nitrogen activity from ($250 < T < 1538\ ^{\circ}C$) is found to be significantly underestimated, beyond the uncertainty range of the calculation, in both phases. The boundary of the α-γ phase change as featured in Lehrer diagrams is calculated within the nitriding potential ($0.001 < r_N < 10$) and temperature ($300 < T < 900\ ^{\circ}C$) ranges. The boundary shows good agreement with experimental data, but the calculated α region is consistently smaller than the data suggests. Motivated by the existence of grain boundaries and other common defects which cause far more unoccupied volume within iron than is expected in idealised lattice structures, the effect of excess vacancy concentrations in varying ranges between $10^{-12} < c_v < 10$ at.% on nitrogen solubility and the α-γ phase change is quantified. It is shown how discrepancies between the theoretical ideal crystal and experimental data can be "corrected" by excess vacancies to model the non-ideality of iron lattices in reality, and evidence is given for the validity of this correction. Results are presented in an applied context, allowing opportunities for experimental verification.

Keywords:
A. metals and alloys, B. solid state reactions, C. atomic scale structure, C. phase transitions, C. point defects, D. thermodynamic modelling

1. Introduction

Nitriding is an important process to increase mechanical strength and wear resistance of metallic work pieces such as cutting blades, gearwheels and crankshafts. By creating an atmosphere with high nitrogen activity, conventional nitriding processes such as gas nitriding and plasma nitriding lead to the formation of a hard surface layer (termed *compound layer*) that is composed of ϵ and γ'-type iron nitrides. A *diffusion layer* which may comprise of nitrides, both in the α and γ matrix is formed underneath the compound layer [1, 2, 3].
Isolated iron which perfectly conforms to a body centered (α-Fe) or face centered (γ-Fe) cubic lattice arrangement does not exist in reality; numerous imperfections in the crystal structure may be observed, even in alloy grades which are processed specifically to maximise purity. In experimental determination of thermodynamic properties (of the iron-nitrogen system [4, 5, 6]), this fact is usually not considered, as high purity samples are generally considered good approximations of perfect purity. However, the difference in thermodynamic behaviour between (theoretical) ideal, high purity and more significantly deformed; subjugated to irradiation, ball-milling or shot-peening for instance; crystal structures is currently uncertain.
Common defects in industrial iron alloy grades, such as grain boundaries, reduce the packing efficiency of iron atoms which means there is excess unoccupied volume within the structure [7]. Due to this, iron alloys in nature may behave as if they are far more vacancy-rich than simulated idealised lattices under the same conditions [8]. Thus, this work explores the case where the concentration of lone vacancies is held fixed out of equilibrium to be far more plentiful.

*Corresponding authors
Email addresses: a.karimi@warwick.ac.uk (Aurash Karimi), m.auinger@warwick.ac.uk (Michael AUINGER)

An otherwise-ideal iron lattice is considered from first principles using Density Functional Theory (DFT) which contains lone nitrogen interstitials, vacancies and nitrogen-(mono)vacancy complexes, as these point defects carry large significance but are relatively simple. It is quite apparent from recent DFT studies that for both α [9, 10] and γ [11, 12] iron phases that octahedral sites in the proximity of vacancies act as trapping sites for nitrogen, which leads to the formation of complexes at thermal equilibrium in quantities far beyond that of lone vacancies. However, current literature lacks quantified evaluations on the potential thermodynamic influences from nitrogen-vacancy complexes in an explicitly applied context, motivating the work that follows.
In this work a thermodynamic model (section 2.2) is used to reassess the solubility and phase stability with an explicit dependence on excess vacancies for the α and γ phases. DFT assessments of the defects considered, which the thermodynamic model depends on, are outlined in section 2.1, which entails the calculation of both internal energy of individual defects and energy barriers of nitrogen diffusion. Preceding this, the methods section opens with a high-level summary of the theoretical considerations in this work, and the notation used throughout.

2. Methods

Model Description and Notation. The nitriding process is modelled by assuming that there is abundant nitrogen at the surface of an iron alloy (due to the high activity of nitrogen) which proceeds into the material via interstitial diffusion [8, 3]. Dissolved nitrogen may then interact with lone vacancies (denoted v) or nitrogen-vacancy complexes (denoted vN_j) where j is the number of nitrogen atoms within the complex. The process is governed by elementary reactions 1 and 2.

$$\frac{1}{2}\,\mathrm{N}_2 \quad \rightleftharpoons \quad [\mathrm{N}] \tag{1}$$

$$[\mathrm{N}] + [\mathrm{vN}_{j-1}] \quad \rightleftharpoons \quad [\mathrm{vN}_j] \tag{2}$$

Let i denote chemical components of reaction 1 or 2 and $s \in \{\mathrm{gas}, \alpha, \gamma\}$ be the state of i, which are diatomic gas, or interstitially dissolved within octahedral sites in either an α or γ phase Fe lattice respectively. $E_i^s(T)$ and c_i^s denote the internal energy and concentration of i in state s respectively. At absolute zero the internal energy E_i^s is defined as $E_i^s(0)$. At thermodynamic equilibrium with fixed temperature and pressure the concentrations are $c_i^{s_{eq}}$.
The rate at which nitrogen enters the proximity of a vacancy from the atmosphere, denoted $r^s_{\mathrm{enter}}(T)$, is the forward rate at which reaction (1 & 2) proceeds. The rate-determining step of this reaction is assumed to be the interstitial diffusion of nitrogen to reach a vacancy, which is the forward reaction of 2, hence $r^s_{\mathrm{enter}}(T)$ is considered to be approximately equal to the forward rate of 1. The opposing rate at which nitrogen leaves the proximity of a vacancy, denoted $r^s_{\mathrm{leave}_j}(T)$, is then a backward rate of reaction 2. Collectively, these rates define the distribution of nitrogen between complex sites, lone nitrogen defects and the gas state at a given temperature. $R = 8.314$ J mol^{-1} K^{-1} is the universal gas constant which is used throughout this work.

2.1. Atomic Scale Modelling

DFT calculations were carried out with the projector augmented wave method as implemented in GPAW [13, 14]. The Perdew, Burke and Ernzerhof (PBE) exchange-correlation functional [15] was used in all plane wave calculations. The atomic software library ASE [16] was used to interface with GPAW. Ferromagnetic (FM) body centered cubic (BCC) Fe and non-magnetic (NM) face centered cubic (FCC) Fe supercells are used as samples of α and γ phase Fe respectively. A full breakdown of parameters used in DFT calculations is given in tables 1 & 2.

The parameters which are chosen for each DFT calculation are the kinetic cut-off energy for plane-wave functions E_{cut}, the number of k-points distributed in the Brillouin zone using the Monkhurst-Pack method [17], the supercell size, and Methfessel-Paxton [18] (first order) smearing. The smearing width is set to 0.1 for all calculations. For non-smearing parameters, an estimate for the maximum residual uncertainty in output energy with respect to each parameter is considered. E_{cut} and k-points are increased until there is < 0.02 eV residual uncertainty for each supercell size considered. Convergence with respect to supercell size requires case-specific treatment as it is the most sensitive trade-off of computational burden against accuracy. (see closing paragraph of sections 2.1.1 and 2.1.2).

Table 1: Parameter sets for the plane wave DFT calculations used in calculation of internal energies. Error and cut off energy values are given in eV. For temperature-dependent values, u is the maximum uncertainty over the largest temperature range used. u values of - are not explicitly calculated but are inferred to be small with respect to total error.

Energy	E_{cut}	u	supercell	u	kpts	u	u_{total}
E^{α}_{N}	900	0.003	4×4×4	0.013	4×4×4	0.014	0.030
$E^{\alpha}_{\text{N}}(T)$		-	3×3×3	0.037 + 0.003	8×8×8	-	0.040
E^{α}_{v}		< 0.001		0.004		< 0.001	0.004
$E^{\alpha}_{\text{vN}_j}$		0.003		0.055		0.008	0.066
$E^{\alpha}_{\text{vN}_j}(T)$		-		0.037 + 0.019		-	0.056
E^{γ}_{N}		0.003		0.018	12×12×12	0.001	0.022
$E^{\gamma}_{\text{N}}(T)$		-		0.023 + 0.003	6×6×6	-	0.026
$E^{\gamma}_{\downarrow}$		< 0.001		0.005		0.009	0.014
$E^{\gamma}_{\text{vN}_j}$		0.003		0.113	12×12×12	0.001	0.117
$E^{\gamma}_{\text{vN}_j}(T)$		-		0.023 + 0.030	6×6×6	-	0.053

Table 2: Parameter sets for the plane wave DFT calculations used in Nudged Elastic Band (NEB) calculations. The remaining uncertainty u in the resulting energy barriers for nitrogen jumps in iron lattices found for each parameter are given in eV. A u value of - is not explicitly known but inferred to be small with respect to total error. E^{s}_{∞} and $E^{\alpha}_{x\to y}$ denote vacancy-free and vacancy-containing supercells in the NEB respectively.

Energy	E_{cut}	u	supercell	u	kpts	u	u_{total}
$E^{\alpha}_{x\to y}$	500	< 0.001	3×3×3	0.009	8×8×8	-	0.010
E^{γ}_{∞}		< 0.001	2×2×2	< 0.001	8×8×8	-	0.001
$E^{\gamma}_{x\to y}$		< 0.001	3×2×2	0.035	6×8×8	-	0.036

2.1.1. Internal Energies

Calculating $E^{s}_{i}(T)$. Let $\tilde{E}(\text{Fe}_n X)$ be the relaxed energy of a DFT supercell with n iron atoms and crystal structure s. Internal energies E^{s}_{i}, which can be considered to correspond to infinitely dilute point defects within the supercell approximation, are calculated using equations 3 to 5:

$$E^{s}_{\text{N}} = \tilde{E}(\text{Fe}^{s}_{n}\text{N}) - \tilde{E}(\text{Fe}^{s}_{n}) \tag{3}$$

$$E^{s}_{\text{v}} = \tilde{E}(\text{Fe}^{s}_{n-1}\text{v}) - \frac{n-1}{n}\tilde{E}(\text{Fe}^{s}_{n}) \tag{4}$$

$$E^{s}_{\text{vN}_j} = \tilde{E}(\text{Fe}^{s}_{n-1}\text{vN}_j) - \tilde{E}(\text{Fe}^{s}_{n-1}\text{vN}_{j-1}) \tag{5}$$

When X is a complex, the energy is dependant on location of the nitrogen atoms relative to the vacancy. In this case, E^{s}_{i} is set to the minimal energy found out of all candidate structures of X tested. The value of $E^{s}_{\text{vN}_j} - E^{s}_{\text{N}}$ gives the reaction enthalpy of reaction 2, which indicates the attractiveness of a complex containing j nitrogen atoms to a lone nitrogen defect. If the reaction enthalpy is large and positive then it is not energetically beneficial for nitrogen to migrate to form that size of vacancy. It is assumed in this work that generally, $E^{s}_{\text{vN}_j} - E^{s}_{\text{N}}$ increases with j for $j > 2$ (following assessments from literature [12, 9]). Based on this assumption the inequality

$$2 < n^{\max_s}_{\text{N}} = j \text{ is the largest integer such that: } E^{s}_{\text{vN}_j} - E^{s}_{\text{N}} < 0.5 \text{ eV} \tag{6}$$

is used to set integer $n^{\max_s}_{\text{N}}$ such that the maximum sized complex considered in a thermodynamic model still has a significant contribution to total nitrogen concentration relative to lone interstitial nitrogen. Complexes more containing more nitrogen atoms than $n^{\max_s}_{\text{N}}$ then need not be considered.

Temperature dependence and zero point energy of E^{s}_{i} for each i containing nitrogen is assumed to primarily consist of vibrational contributions, where each nitrogen atom is approximated to behave as a three dimensional harmonic oscillator. Vibrational frequencies are calculated within a supercell representing i by making small displacements to each nitrogen atom and using the resulting energies to assemble a Hessian matrix, resulting in a second order approximation of force constants. This method was used as it is implemented in the ASE software library [16].

Convergence. The degree of convergence of equation 3 with respect to (the number of iron atoms) n for both BCC (n = 2, 16, 54, 128) and FCC (n = 4, 32, 108) crystal structures in cubic supercells is observed with two approaches. In the more commonly used (and computationally cheaper) constant volume (CV) approach the lattice parameter is minimised using the smallest possible cubic supercell of iron and this lattice parameter is held fixed for each larger supercell. The constant pressure (CP) approach accounts for changes in supercell volume due to point defects by recalculation of the stable lattice parameter at each supercell size. The CV and CP values are two candidate values which can be equated to E^s_{N}, so the method which results in the smallest energy difference between the two largest considered supercell sizes is chosen as the final result. Furthermore, a quasi-harmonic approach where 4 sets of vibrational frequencies were calculated at 4 different supercell volumes about the energy minimum was used to determine the impact of thermal expansion on internal energies. The convergence behaviour of adding nitrogen to a complex in a supercell is assumed to be similar to adding a lone nitrogen defect to conserve computing resources, so nitrogen-containing supercells in equation 5 are only considered at a single volume. For n smaller than that used to determine the converged E^s_{N}, a more precise definition of equations 3 and 5 may be obtained by fitting convergence data from the CV approach. Namely, an extra term

$$E^s_{\mathrm{repulse}}(n) = a\frac{\log n}{n^3} + b\frac{\log n}{n^2} + c \tag{7}$$

is added to each equation, which outputs an estimate for the energy difference at n between the true internal energy and the converged 'infinitely dilute' supercell energy. In this study $E^s_{\mathrm{repulse}}(n)$ is only calculated for lone nitrogen defects within α or γ (see table 3), otherwise $E^s_{\mathrm{repulse}}(n) = 0$.

Table 3: Parameters for fitting equation 7, where the output energy may either be in eV or kJ mol^{-1}

defect		a		b		c		range
phase	species	eV	kJ mol^{-1}	eV	kJ mol^{-1}	eV	kJ mol^{-1}	
α	N	-27.27	-2631	57.66	5564	-0.002417	-0.2332	2 < n < 128
γ	N	23.82	2298	26.39	2547	-0.006228	-0.6009	4 < n < 108

2.1.2. Rates of Reaction

Energy Barriers. Nudged elastic band (NEB) [19] calculations were used to calculate energy barriers for nitrogen jumps between interstitial sites both with and without a vacancy present in the supercell. In all cases the NEB images are relaxed with the BFGS algorithm as implemented in ASE until the overall forces are less than 0.5 eV, then climbing image NEB [20] is used with the FIRE relaxation algorithm [21] until the forces are less than 0.025 eV. The energy barrier for a transition between adjacent stable octahedral positions is denoted by $E^s_{x\to y}$. Sites for nitrogen are defined by their distance from a vacancy, so that o^s_j is the j^{th} nearest neighbour to a vacancy. In the case of ideal crystals, each jump between sites is identical, so only one barrier $E^s_{\infty\to\infty} := E^s_{\infty}$ needs to be calculated. Close to a vacancy there is far less symmetry between different sites, so at least one barrier should be defined for each j (see figure 1).

Rates. Reaction rates are defined in the form of

$$r^s_{\mathrm{enter\,/\,leave}}(T) = e^{A-\frac{B}{RT}} \tag{8}$$

The jump rate of nitrogen from x to y is defined by the equation

$$r^s_{x\to y}(T) = \upsilon^s_{x\to y} e^{-\frac{E^s_{x\to y}}{RT}} \tag{9}$$

where $\upsilon_{x\to y}$ is the product of vibrational frequencies of nitrogen in the x position divided by the product of vibrational frequencies in the transition state. Due to symmetrical energy barriers in the ideal crystal, A and B values from equation 8 follow immediately from equation 9. For the non ideal case, the rejection-free variant of the Kinetic Monte Carlo (KMC) algorithm is used to generate trajectories which are used to adapt the asymmetrical jump rates (see table B.6) in the proximity of a vacancy so that the net rate at which nitrogen leaves vacancies can be calculated. Nitrogen is evolved in a trajectory within a cubic simulation box which is made to be as small as possible while still

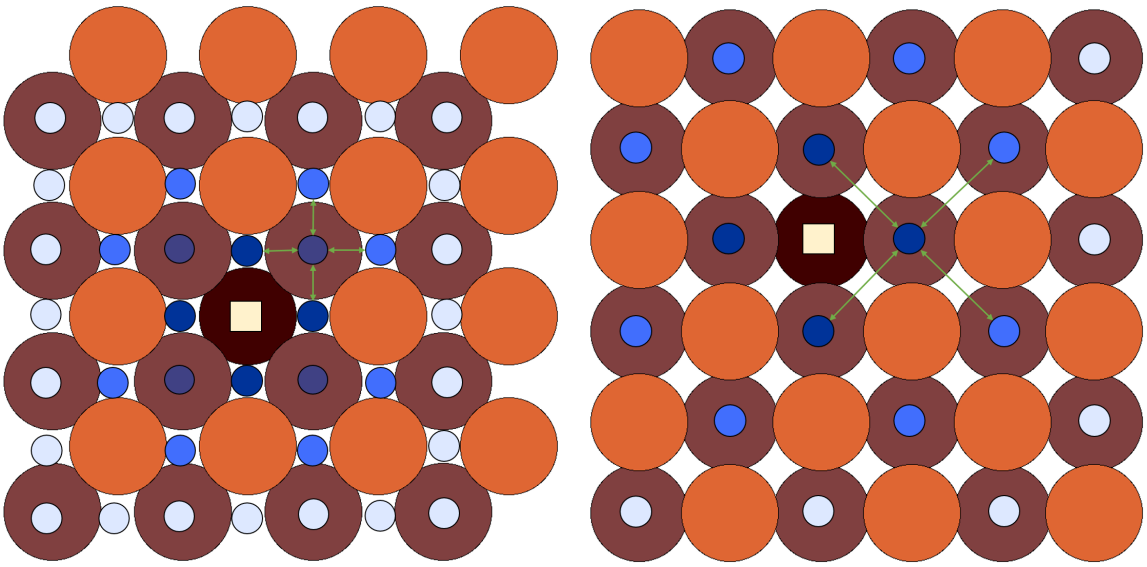

Figure 1: A two-dimensional cross section showing octahedral sites for nitrogen atoms (small circles) within α-Fe (BCC, left) and γ-Fe (FCC, right) lattices of iron atoms (large circles) in the proximity of a vacancy (yellow square). Green arrows represent the jumping directions for nitrogen atoms between sites, which are considered to happen with equal frequency if both ends of the arrow point to the same type of site (shade of blue). The small circles with the darkest shade of blue are the sites which are most influenced by the vacancy, whereas the lightest shade indicates sites which are far enough from the vacancy so that the energy barriers between them are not effected.

containing every type of o_j^s site for which the energy barriers are calculated. The trajectories allow for the calculation of displacement of nitrogen over time at a given temperature. Over a calculated temperature range a linear fit is created from KMC results to calculate A and B.

Convergence. The largest m×m×m or m+1×m×m sized supercells which are possible within computational constraints are used during NEB calculations. In the cuboid supercells, the NEB calculation is oriented so that the largest distance between the initial and ending states are in the periodic $m+1$ direction to minimise symmetry. For a chosen m it is then necessary to decide the maximum number of o_j^s sites which can be considered. Considering more sites provides more energy barriers to calculate rates, but sites which are further away from the vacancy tend to have increased symmetry between periodic images, leading to a decrease in the accuracy of energy barriers. It is immediately clear that j should satisfy $j < \frac{m+1}{2}$, as larger j would result in overlapping site definitions when considering periodicity. It is also ensured that each j satisfies the inequality equation 10.

$$E^s_{j\to(j+1)} - E^s_{j\to(j-1)} > 0 \tag{10}$$

Equation 10 is based on the intuition and previous findings that nitrogen moving towards a vacancy has lower energy barriers than when it is moving away from it. If the inequality is not satisfied, then it would appear that the influence of symmetry is large enough so that E^s_∞ is closer to the true barrier than $E^s_{j\to(j+1)}$, so it is more beneficial to accuracy to treat the site as uninfluenced by the vacancy.

2.2. Thermodynamic Model

Gibbs Free Energy. At fixed temperature T and pressure p, the equation

$$G(T,p) = \sum_{\text{(i, s)}\in\text{reaction}} g(c_i^s, T, p) \tag{11}$$

is defined such that $\frac{\partial g}{\partial c_i^s} = \mu_i^s$, where μ_i^s is the molar chemical potential of i in state s. Thus, the derivative ΔG may represent the Gibbs Free Energy change (of reaction) for reactions 1 and 2. For the purposes of this work, the pressure

dependency of equation 11 in the gas phase can be reduced to just a dependence on the nitrogen partial pressure p_{N_2} with reference pressure $p_0 = 1$ atm [2]. Ammonia is commonly used to create the high nitrogen activity required to dissolve nitrogen in iron in significant quantities. Thus, the partial pressure of nitrogen at fixed temperature can be expressed using the nitriding potential r_N. This is portrayed using the equation

$$p_{N_2} = p_0 \left(r_N e^{13.955 - \frac{6498.0}{T}} \right)^2 \tag{12}$$

which adapts gas equilibrium data for ammonia from [2].

N_2 is treated as a linear ideal gas in order to calculate it's temperature dependent Gibbs Free Energy from first principles using equation

$$g^{\text{gas}}(c_N^{\text{gas}}, T, p_{N_2}) = \frac{1}{2} c_N^{\text{gas}} \left[E_{N_2}^{\text{gas}}(0) - RT \left(S_{\text{other}} + S_{\text{translational}} ln \left(\frac{p_{N_2}}{p_0} \right) \right) \right] \tag{13}$$

The entropy components denoted by S may be calculated from the vibrational frequencies of the nitrogen molecule. Configurational entropy of lone nitrogen defects dissolved within iron is defined by

$$S_{\text{config}}(c, k) = c \; ln \left(\frac{c}{k} \right) + (k - c) \; ln \left(1 - \frac{c}{k} \right) \tag{14}$$

Where c is the ratio of interstitial elements to iron atoms, and k is the number of interstitial positions per iron atom. Equation 14 may be used in a more general definition of configurational entropy for an arbitrary nitrogen and/or vacancy containing defect.

$$S(c_i^s, k) \begin{cases} S_{\text{config}}(c, 1) & n_N^i = 0 \\ S_{\text{config}}(c, k) & n_v^i = 0 \\ S_{\text{config}}(c, 1) - c \; ln \left(n_{\text{permute}}^{n_N^i} \right) & n_v^i = 1, n_N^i > 0 \\ 0 & \text{otherwise} \end{cases} \tag{15}$$

Where n_N^i denotes the number of nitrogen atoms within i, $n_v^i \in \{0, 1\}$ the number of vacancies and $n_{\text{permute}}^{n_N^i}$ is the number of energetically degenerate ways the n_N^i nitrogen atoms may be arranged within the defect. The molar Gibbs Free Energy for a defect with known internal energy (see section 2.1.1) is expressed by

$$g(T, c_i^s) = c_i^s \left(E_i^s(T) + E_{\text{repulse}}^s \left(\frac{1}{c_i^s} \right) \right) + RTS(c_i^s, k) \tag{16}$$

Under the considered range of conditions, the number of defects is not necessarily dilute with respect to the amount of Fe atoms. The significant difference in internal energy caused by repulsion of nitrogen atoms as the concentration increases past around 1 at.% is approximated by the E_{repulse}^s using fitted parameters (for each s) from table 3 (see section 2.1.1 for calculation details).
With equations 13 and 16, g is now defined for each possible i and s combination considered in this work where the defect is present in an arbitrary concentration.

Molar Fractions. If the individual concentrations of each defect considered is known, one may calculate the molar fraction x_x^s of $x \in \{N, v\}$ using the equation

$$x_x^s = \frac{1}{1 + (c_x^{s_{\text{eq}}} + \sum_i^{n_x^i > 0} n_x^i c_i^s)^{-1}} \tag{17}$$

Calculating $c_i^{s_{eq}}$ for each i is equivalent to solving the optimisation problem

$$\min_{c_i^s} G(T, p) \text{ subject to: } c_{N_2}^{\text{gas}} + c_N^{s_{\text{eq}}} = 1 \tag{18}$$

The constraint in equation 18 is physically motivated, with it's purpose to ensure that the concentration of nitrogen available to facilitate reaction 2 is the exactly the amount removed from the atmosphere by reaction 1 per mole of iron

present. Let P^s_{v} be defined so that $P^s_{\mathrm{v}} c_{\mathrm{v}}^{s_{\mathrm{eq}}}$ is the concentration of vacancies available for reaction 2. Since the formation of the most abundant nitrogen-vacancy complexes is highly favourable if both reactants are in close proximity, it is assumed that the limiting aspect of their formation in the presence of excess vacancies ($P^s_{\mathrm{v}} >> 1$) depends on the interstitial diffusion rate of nitrogen. Hence, diffusion (reaction) rates are used to determine equilibrium concentrations of nitrogen-vacancy complexes as opposed to their internal energies. To this end $\hat{c}^s_{\mathrm{vN}_j}$ is defined using the mass-action law applied to reaction 2 for successive j (equation 20):

$$\hat{c}^s_{\mathrm{vN}_j} = \frac{\left(r^s_{\mathrm{enter}}\right)^j}{\prod_{m=1}^{m=j} r^s_{\mathrm{leave}_m}} \left(c^s_{\mathrm{N}}\right)^j \tag{19}$$

To investigate the thermodynamic behaviour that occurs when there are excess lone vacancies are present initially, but they aren't readily replenished while the system reaches a (meta)stable state, it should be the case that $\sum_j c^s_{\mathrm{vN}_j} \leq P^s_{\mathrm{v}} c_{\mathrm{v}}^{s_{\mathrm{eq}}}$. Thus, the equation

$$c^s_{\mathrm{vN}_j} = P^s_{\mathrm{v}} c_{\mathrm{v}}^{s_{\mathrm{eq}}} \frac{\hat{c}^s_{\mathrm{vN}_j}}{\sum_j \hat{c}^s_{\mathrm{vN}_j}} \tag{20}$$

is used to obtain the concentration of each nitrogen-vacancy complex.

Phase Change. The thermal stability of nitrogen within the α and γ phases relative to the reference state of nitrogen gas at fixed T and p_{N_2} is defined by

$$F(T, p_{\mathrm{N}_2}, c^s_{\mathrm{N}}, c^s_{\mathrm{v}}) = g(c^s_{\mathrm{N}}, T) + \sum_{j=1}^{n_{\mathrm{N}}^{\max_s}} g(c^s_{\mathrm{vN}_j}, T) - g^{\mathrm{gas}}(c^s_{\mathrm{N}} + \sum_{j=1}^{n_{\mathrm{N}}^{\max_s}} c^s_{\mathrm{vN}_j}, T, p_{\mathrm{N}_2}) \tag{21}$$

Where $n_{\mathrm{N}}^{\max_s}$ corresponds to the maximum number of nitrogen considered for complexes in lattice s. Using equation 21 one may identify one of T, p_{N_2}, P^{α}_{v} or P^{γ}_{v} at which the α-γ phase transition occurs by fixing the other three. For example, to solve for a phase change temperature $\hat{T}$:

- Calculate $c_{\mathrm{N}}^{\alpha_{\mathrm{eq}}}$ and $c_{\mathrm{N}}^{\gamma_{\mathrm{eq}}}$ by applying 18 to the sum of equations 16 and 13
- Let $c^{\alpha}_{\mathrm{N}} = c^{\gamma}_{\mathrm{N}} = max(c_{\mathrm{N}}^{\alpha_{\mathrm{eq}}}, c_{\mathrm{N}}^{\gamma_{\mathrm{eq}}})$
- $\hat{T}$ is a root of the equation

$$F(T, p_{\mathrm{N}_2}, c^{\alpha}_{\mathrm{N}}, c^{\alpha}_{\mathrm{v}}) + \frac{1}{2}[2 - (\mathrm{x}^{\alpha}_{\mathrm{v}} + \mathrm{x}^{\gamma}_{\mathrm{v}})](E^{\alpha}_{\mathrm{Fe}}(T) - E^{\gamma}_{\mathrm{Fe}}(T)) = F(T, p_{\mathrm{N}_2}, c^{\gamma}_{\mathrm{N}}, c^{\gamma}_{\mathrm{v}}) \tag{22}$$

where $E^s_{\mathrm{Fe}}(T)$ is the molar Gibbs Free energy of pure Fe, adapted from [22] in this work.

3. Results and Discussion

3.1. Atomic Scale Results

The lattice parameters for ferromagnetic BCC and non-magnetic FCC iron were found to be 2.838 Å(=0.2838 nm) and 3.461 Å(=0.3461 nm) respectively, with negligible discrepancies for both lattice parameters within previous published DFT literature (see [9, 23] and [24, 11] respectively). In comparison to experimental data [25], the lattice parameter for γ Fe at absolute zero is underestimated by non-magnetic FCC Fe by around 0.11 Å (=0.011 nm), whereas the discrepancy for α Fe is < 0.001 Å (=0.0001 nm). The more significant discrepancy in the γ case is not too surprising, Austenite is known to be both paramagnetic and unstable at absolute zero temperature, both of which are not accounted for in the applied DFT methodology.

3.1.1. Internal Energy

Internal energies at absolute zero temperature calculated in this work are presented in table 4, along with total projected uncertainties with respect to convergence of DFT parameters. A large plane wave cutoff energy E_{cut} value was used in this work relative to other DFT publications (900 eV in this study and 500 ±100 eV in others), which is predicted to correspond to discrepancies of around 0.05 eV (α) and 0.08 eV (γ) in nitrogen-containing defect energies between this work and other literature. There does not currently appear to be a widespread consensus within literature of k-points (relative to supercell size) as in the E_{cut} case, so it is more difficult to predict potential discrepancies in this case. However, halving the number of k-points in each cartesian direction as used in this work amounts to energy differences of at most around 0.1 eV, and the majority of k-point meshes used historically fall within this range. It is common to observe supercell sizes identical to those used in this study or one cubic degree larger (see [26, 12]),so the resulting discrepancies between this work and others due to supercell size should not exceed the uncertainty estimates in table 4. For E^{α}_{N} and E^{γ}_{N}, the uncertainties (± 0.070 eV and 0.048 eV respectively) are relatively insensitive to supercell size. This is because they were calculated using the computationally intensive approach of allowing the lattice parameter to vary at each supercell size. As seen in table 4, the uncertainty for internal energies of nitrogen complexed with vacancies can be several times higher, as they were calculated at fixed lattice parameters and are therefore more sensitive to supercell size. When calculation uncertainty in this work is combined with all the preceding considerations, most literature values fall within the anticipated range of values in this work, which amounts to around ±0.2 eV (= 19.3 kJ mol^{-1}) on average.

Incorporating thermal expansion through the quasi-harmonic approach to calculate the temperature-dependant parts of internal energy was compared to calculating temperature-dependence at the energy minimising volume. Over the 523-1394 K range there were maximum discrepancies of around 0.003 eV per atom for both α and γ. Furthermore, considering three volumes instead of four results in a discrepancy of the same order, so incorporating more volumes when fitting the lattice parameter at each temperature was not considered necessary. The small discrepancy between the single and four-volume cases is due to very minimal lattice expansion found due to the vibrational energy of nitrogen (< 0.001 Å) over the temperature range for both α and γ).

It is noteworthy that in this work and other referenced DFT literature, both E^{α}_{v} = 2.22 eV and E^{γ}_{v} = 2.42 eV are significantly overestimated by their experimental evaluations found with positron annihilation, which are 1.4 ±0.1 eV and 1.7 ±0.2 eV [27] respectively. This supports the earlier prediction of this work, which was that real alloys will have far larger vacancy concentrations than would be expected from idealised iron lattices at thermal equilibrium. Henceforth in this work it is set that $n^{\max_s}_{\text{N}} = 3$, which satisfies equation 6 for both s. Due to the large increase in internal energy from $E^{s}_{\text{vN}_2}$ to $E^{s}_{\text{vN}_3}$ values, earlier assertions that complexes with 2 or less nitrogen atoms tend be to far more abundant than the more nitrogen-rich complexes appear to be true.

3.1.2. Rates of Reaction

The intuition that vacancies tend to trap diffusing nitrogen atoms appears to hold true in both α and γ Fe, with the vacancy having a particularly large effect on the barriers between o^{s}_{1} and o^{s}_{2} sites, causing them to deviate greatly from the ideal crystal activation energy E^{s}_{∞}. The maximum number of sites satisfying equation 10 was found to be 3 for the α phase and 2 for γ using 4x3x3 and 3x2x2 supercells. The difference in the value of $E^{s}_{1\to2} - E^{s}_{2\to1}$ between the two largest tested supercells is a good upper bound for uncertainty, as the closest barriers to the vacancy have the largest deviations from E^{s}_{∞} and hence the largest potential for error. The corresponding differences are 0.009 and 0.045 eV for the α and γ phases respectively, so the uncertainty holds some significance in the γ case. It appears that the higher symmetry in the o^{γ}_{2} position for the 2x2x2 cell has caused a high variance in the supercell convergence between different barriers, by underestimating the energy minimum at o^{γ}_{2} and hence widening the energy barrier $E^{\gamma}_{2\to1}$. Therefore, a moderate increase in accuracy should be achieved in the γ if a larger supercell size can be used within computing constraints. This indicates that while equation 10 is a good overall marker of how many energy barriers can be calculated for a given supercell, it does not necessarily ensure the energy barriers are precise to a level of experimental uncertainty (< 0.01 eV). Between o^{α}_{3} and o^{α}_{4} sites the energy barriers do not deviate largely from E^{α}_{a}, which indicates that at this distance the effect of the vacancy on barriers is largely diminished. Thus, larger supercells to calculate barriers for further positions from the vacancy most likely need not be considered even if computing resources are abundant. In the γ case, using a 2×4×3 supercell which is quite taxing on computing resources still leaves too much symmetry to satisfy equation 10, as $E^{\gamma}_{2\to3} - E^{\gamma}_{3\to2}$ = -0.036 eV with this supercell. Employing larger supercells to calculate these barriers may prove beneficial to accuracy, although it is not expected that the energy

Table 4: The calculated Internal energies at zero Kelvin of a singular nitrogen atom or vacancy in various point defects within iron, with corresponding uncertainty estimates and zero-point energies (of nitrogen only).The reference state for each internal energy is that of the full supercell containing the defect, and the tabulated value is the energy which remains (see equations 3-5) when a single nitrogen atom is left. For instance, considering the nitrogen-vacancy complexes, the associated internal energy is of the nitrogen atom which is added to form $E^s_{\mathrm{vN}_j}$ from $E^s_{\mathrm{vN}_{j-1}}$. Identified DFT literature sources are added for comparison, which are adjusted where required using $E^{\mathrm{gas}}_{\mathrm{N}_2}$ in this work so that all values share a common reference state. Abbreviations in parenthesis refer to magnetic states where the magnetism is different to that used in this work.

Defect	Energy		Uncertainty (±)		Zero-point Energy		Literature
	eV	kJ mol^{-1}	eV	kJ mol^{-1}	eV	kJ mol^{-1}	eV
$\frac{1}{2}E^{\mathrm{gas}}_{\mathrm{N}_2}$	-8.450	-815.1	-	-	0.146	14.1	
E^{α}_{N}	-8.198	-791.0	0.070	6.75	0.0982	9.48	-8.13 [28], -8.43[23], -8.317 [26]
E^{α}_{v}	2.22	214.2	0.004	0.39	-	-	2.12 [9]
$E^{\alpha}_{\mathrm{vN}_1}$	-9.080	-876.1	0.112	10.81	0.0894	8.63	-8.91 [9]
$E^{\alpha}_{\mathrm{vN}_2}$	-8.930	-861.6	0.112	10.81	0.0945	9.1	-9.02 [9]
$E^{\alpha}_{\mathrm{vN}_3}$	-7.863	-758.7	0.112	10.81	0.0998	9.63	-7.93 [9]
E^{γ}_{N}	-8.768	-846.0	0.048	4.63	0.128	12.3	-8.609(AFMD) [12]
E^{γ}_{v}	2.42	233.5	0.014	1.35	-	-	2.30 [11] 2.23 [24]
$E^{\gamma}_{\mathrm{vN}_1}$	-9.486	-915.2	0.170	16.40	0.129	12.5	-9.468 [11]
$E^{\gamma}_{\mathrm{vN}_2}$	-9.497	-916.3	0.170	16.40	0.126	12.1	-9.578 [11]
$E^{\gamma}_{\mathrm{vN}_3}$	-8.776	-846.7	0.170	16.40	0.120	11.6	-8.848 [11]

difference in barriers at o^{γ}_3 would be as significant as the difference at o^{α}_3 due to further distance from the vacancy in the γ case. Indeed, the slow supercell convergence is a sign that the true $E^{\gamma}_{2\to3} - E^{\gamma}_{3\to2}$ is relatively small in magnitude, as it is unable to outweigh the effect of symmetry even in relatively large supercells.

Table 5: Reaction rates calculated in this work as defined by equation 8. j indicates the number of nitrogen atoms in the associated complex. * indicates estimated errors deduced from similar calculations

Rate			A	B		Uncertainty (±)	
Direction	phase	j		eV	kJ mol^{-1}	eV	kJ mol^{-1}
enter v	α	-	-5.624	0.727	70.1	0.010	1.0
	γ	-	-4.064	2.247	216.8	0.036	3.5
leave v	α	1	-1.990	1.734	167.3	0.019	1.8
		2	-1.990	1.574	151.9	0.019	1.8*
		3	-1.990	0.528	50.9	0.019	1.8*
	γ	1	-1.583	2.811	271.2	0.045	4.3
		2	-1.583	2.839	273.9	0.045	4.3*
		3	-1.583	2.062	198.9	0.045	4.3*

3.2. Thermodynamic Implications

3.2.1. Solubility

Idealised Iron. The presence of lone nitrogen and vacancies within iron leads to the formation of complexes by reaction 2, and provided there is plentiful nitrogen available at the metal surface, increases the total fractions of nitrogen and vacancies in the system at equilibrium. It is seen from figure 2 that in both iron phases the total fraction of vacancies (equation 17) is heavily dependant on the nitriding potential and temperature, and many orders of magnitude above $c^{s_{\mathrm{eq}}}_{\mathrm{v}}$. This relationship agrees with findings in previous work [29] (α-Fe) and [11] (γ-Fe). The dependence on r_{N} is far stronger in the α case, showing that there is a stronger tendency to form complexes in this phase, which can also be surmised from comparing the internal energies.

The same does not hold for the total fraction of nitrogen, as an insignificant fraction of the nitrogen dissolved within either Fe phase is contained in complexions with vacancies, compared to the amount of lone nitrogen interstitial defects. This is to be expected considering the definition of complex concentrations (equation 20), the product $c^{s_{\mathrm{eq}}}_{\mathrm{v}} c^{s_{\mathrm{eq}}}_{\mathrm{N}}$

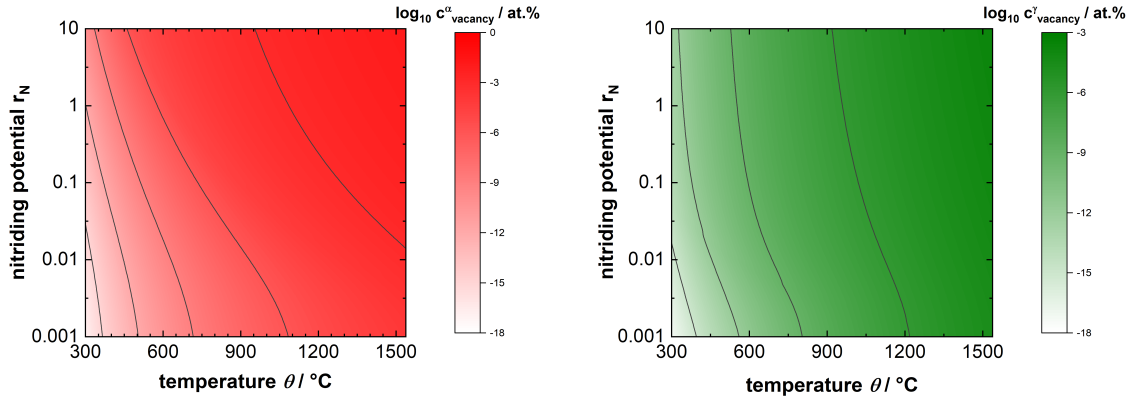

Figure 2: The fraction of vacancies in idealised α (left) and γ (right) iron when nitrogen-vacancy complexes are considered as well as lone vacancies. Note that the upper limit of vacancies reached under these conditions is lower in the γ case and this is reflected in the colour bar axis.

tends to be far smaller than $c_{\mathrm{N}}^{s_{\mathrm{eq}}}$, but relatively close to $c_{\mathrm{v}}^{s_{\mathrm{eq}}}$. Indeed, for hydrogen [24], carbon [30] and previous (γ) nitrogen studies [11] the relationship found between the concentrations of interstitial elements, vacancies (at thermal equilibrium), and their complexes are very similar to the relationship discussed here. The calculated solubility of nitrogen at $p_{\mathrm{N}_2} = 1$ atm up to the melting point of Fe is shown in figure 2 (left). In line with the previous comments, the fraction at equilibrium is almost entirely comprised of lone nitrogen interstitials, meaning that vacancies have little influence on nitrogen solubility at equilibrium. This matches the conclusion from [9] for α-Fe whereas a similar explicit comparison for γ-Fe was not found. In comparison with experimental results (sourced from [25, 31]), there are underestimations in nitrogen solubility beyond the predicted uncertainties in the DFT results of up to an order of magnitude for both phases. If an idealised crystal may indeed be used to calculate the solubility of nitrogen at the same precision of experiments, then the underestimations in $E_{\mathrm{N}}^{s}(T)$ would likely be due to unconsidered temperature-dependant effects. In a sensitivity analysis, a normal distributed error term ($\sim \mathcal{N}(0, 10)$) was added to $E_{\mathrm{N}}^{s}(T)$ (using the lower uncertainty bound energy value at $T = 0$) at evenly spaced intervals over the stable temperature ranges of each phase to create 10000 independent samples. This resulted in 6.84% and 14.5% of the sample solubility's for α and γ respectively exceeding a linear fit of experimental solubility results (on average over the temperature ranges), which corresponds to average over-estimations of internal energies of around 14.9 and 10.5 kJ mol^{-1}. Whilst this magnitude of error is not impossible through systemic DFT errors, phonon energies and magnetic considerations which have not been accounted for in the model, the large and consistent (over both phases) overestimation of energy gives cause to investigate the vacancy-rich case.

Iron with Excess Vacancies. Since vacancies tend to make the dissolution of nitrogen more favourable, the solubility of nitrogen increases when they are in excess. This relationship is depicted in figure 2 (right) for $p_{\mathrm{N}_2} = 1$ atm. It is observed that experimental α solubility values fall within the $0.001 < c_{\mathrm{v}}^{\alpha} < 0.1$ at.% whereas for the γ and δ values $1 < c_{\mathrm{v}}^{\gamma}, c_{\mathrm{v}}^{\delta} < 10$ at.%. However, the uncertainty from DFT calculations remains, as well as the assumptions of the thermodynamic model, so a discrepancy between calculated concentrations vacancy and the true concentrations of an order of a magnitude would not be too surprising. The higher temperature phases appear to contain significantly more vacancies than nitrogen atoms. As the temperature increases, nitrogen is increasingly mobile and has the thermal energy to escape vacancy sites more easily and the trapping effect is weaker. This is observed concretely through the term $\frac{(r_{\mathrm{enter}}^{s})^{j}}{\prod_{m=1}^{m=j} r_{\mathrm{leave}_m}^{s}}$ in equation 20, which tends towards 1 as $T \to \infty$. Particularly at higher temperatures, the expected proportion of excess vacancies appear to make up a substantial proportion of the metal, which may correspond to the large coverage of the interior by grain boundaries and other defects. One may make the general observation that the number of excess vacancies predicted by experimental data in figure 2 is increasing with temperature in each phase. It appears that at lower temperatures nitrogen is less efficient at interacting with vacancies which are suggested to be available at higher temperatures. Finer grain boundaries and stronger vacancy traps could obstruct uniform access to all vacancies for nitrogen at low temperatures, meaning that less vacancies can be "frozen in" to the lattice by nitrogen

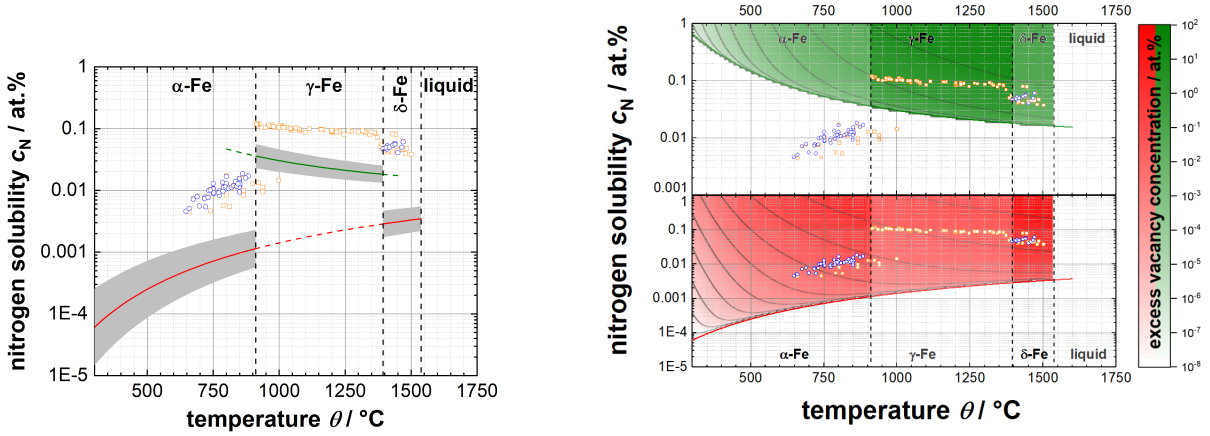

Figure 3: Solubility of nitrogen in iron at nitrogen partial pressure $p_{N_2} = 1$ atm. Experimental values are represented by blue circles [25] and orange circles [31]. In the left image, the solubility of nitrogen in ideal crystals as calculated by DFT is depicted for α (red line) and γ (green line) iron, and DFT calculation uncertainty is represent by the grey shaded area. Excess vacancies, represented by red and green contours, are added to α and γ respectively in right image which increases the solubility of nitrogen above the value obtained from an ideal crystal calculation.

in a given time span. Contrary logic would explain why there is a jump in predicted excess vacancies from the α phase to the γ phase. While diffusion in the γ phase is known to be slower in general, the traps are significantly weaker while the grain boundaries are coarser meaning diffusion directions should be less constrained by vacancies. Indeed, it is assumed that r^s_{enter} is equal the unhindered diffusion rate of nitrogen in the base metal, but in reality imperfections in the crystal structure may inhibit nitrogen atoms from reaching more stable configurations because their access to available vacancies is restricted. At higher temperatures (around 912 $°C$), the variation of excess vacancies with respect to temperature changes reduces sharply, indicating that available vacancies are utilised to a a maximal value. This would explain both the higher variance in the predicted number of vacancies filled, and the increased sparsity of experimental data in the α phase, as less vacancies are required to make relatively large changes to solubility.

3.2.2. Phase Stability

Idealised Iron. As seen in figure 4, the α-γ phase boundary appears to strongly resemble the line obtained from experimental data (FSstel accessed via FactSage [32]). It is not too surprising that the phase boundary is a better fit to experimental data than the calculated nitrogen solubilities at $p_{N_2} = 1$. As the solubility results are underestimated for both phases this leads to consistent changes in energy for both phases in equation 21, so that while absolute energies for each phase may be overestimates of experimental energies, the discrepancy is largely cancelled in the phase boundary computation.

If the $E_{\text{repulse}}(n)$ terms are omitted when calculating the phase boundary, it appears that at lower temperatures and larger r_N the calculated boundary diverges from the experimental data. It seems that the unconstrained internal energy is an under-estimate, so that it results in over-estimations in the value of $c_N^{\gamma_{eq}}$. This is directly linked to supercell convergence, using energy which is not corrected for repulsion in calculating equilibrium concentrations diverges from the true concentration as it increases past the supercell size (i.e for $c_N^{\gamma_{eq}} > \frac{1}{109} \approx 0.0091$) from which the energy originates. The $E_{\text{repulse}}(n)$ terms are extrapolated outside the range prescribed in table 3 to $n = 200$, otherwise a pronounced kink is created in the phase boundary, due to the relatively sudden drop in the derivatives (with respect to r_N and T) of $c_N^{\gamma_{eq}}$. A small kink remains in figure 4 at around 780 $°C$, but it was not deemed necessary to extrapolate to larger n. The thermodynamic model is significantly more (computationally) costly when the repulsion terms are included, and the uncertainty in extrapolation increases with n. It is likely that using information from larger supercells to fit the repulsion energy and expand the range of the repulsion function would result in a smoother (and slightly more accurate) phase boundary if required.

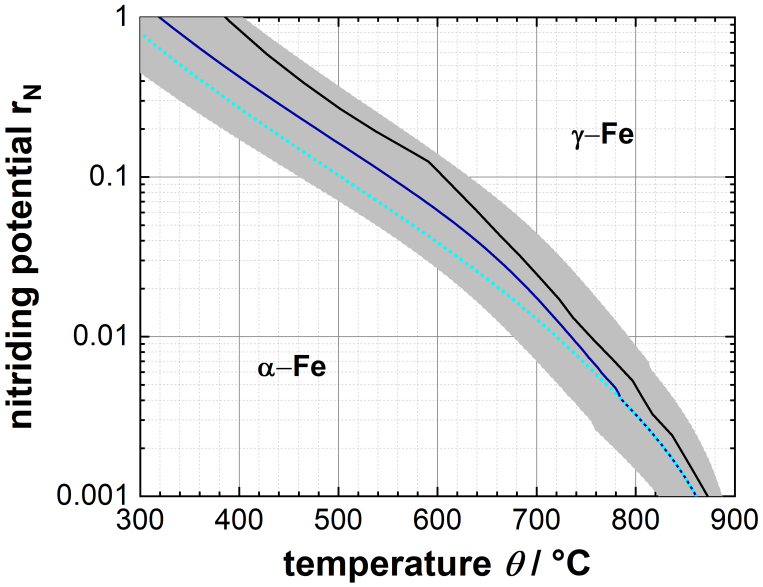

Figure 4: The calculated α-γ phase boundary in the iron-nitrogen system from first principles (blue line) with a corresponding uncertainty range (grey area)). The cyan dots represent the calculated boundary line when the repulsion of dissolved nitrogen atoms is not accounted for in the thermodynamic model. The black line is the corresponding fit of the boundary line from experimental data (sourced from the FSstel database accessed via FactSage [32]). Although in reality there are more stable iron-nitride allotropes in certain regions for the conditions featured, they are not included in this figure for conciseness.

Iron with Excess Vacancies. Since nitrogen-vacancy interactions are energetically favourable, the α-γ phase boundary can become more favoured towards the α-phase or γ-phase (see figure 5) when vacancies are in excess in the respective phases. The thermodynamic model does not take into account the repulsion of nitrogen between complexes, meaning that the total nitrogen fractions within vacancies are expected to be overestimates when a substantial amount of the total nitrogen is contained within them and the total fraction of vacancies is large (> 1 at.%). The attraction of nitrogen-vacancy complexes between each other to form larger complexes, which competes with the repulsion of the contained nitrogen atoms is a relationship which is still under investigation in literature [11, 12, 9], so it is difficult to predict the point at which vacancy complexes will cease to form due to unfavourable repulsion (despite an abundance of vacancies and nitrogen). Nevertheless, the majority of regions in figure 5 (left) should not suffer significant inaccuracies from this, as the regions of the Lehrer diagram with high nitriding potential and temperature tend to contain the largest total fractions of vacancies (see figure 2).

Nitriding conditions commonly have a nitrogen activity which greatly exceeds p_{N_2} = 1 atm, due to abundant nitrogen, nitrogen-vacancy complexes form quickly and most excess vacancies will contain nitrogen when a metastable state is reached. With reference to figure 5, following the contour surface edges to the bottom right from the α-γ-γ' triple point ($r_N = 0.124$, $T = 592°C$), increasingly more vacancies are required to make a noticeable difference to the phase boundaries. As can be seen in figure 6, the surface closest to the triple point is heavily shaded, as a larger range of excess vacancies (with smaller concentrations) may alter the phase change than in the less nitrogen rich surfaces. It is noteworthy that closer to the triple point the phase change is more sensitive to excess vacancies, because the largest deviations from experimental data (see figure 4) are also increasing towards the triple point. Due to higher effectiveness of vacancies as traps in the α case relative to γ, the surfaces in figure 6 are dominated by positive values, meaning that non-ideal of crystals are more likely to favour a larger α phase region. True to this logic, there is consistently an underestimation of the α phase region by the ideal crystal calculation. On the other hand, the temperature difference between the α-γ boundary calculated in this work compared to the experimental data by no more than 80 $°C$ (up to the triple point). It seems that with regards to phase boundary, in contrast to calculations of nitrogen solubility, the ideal

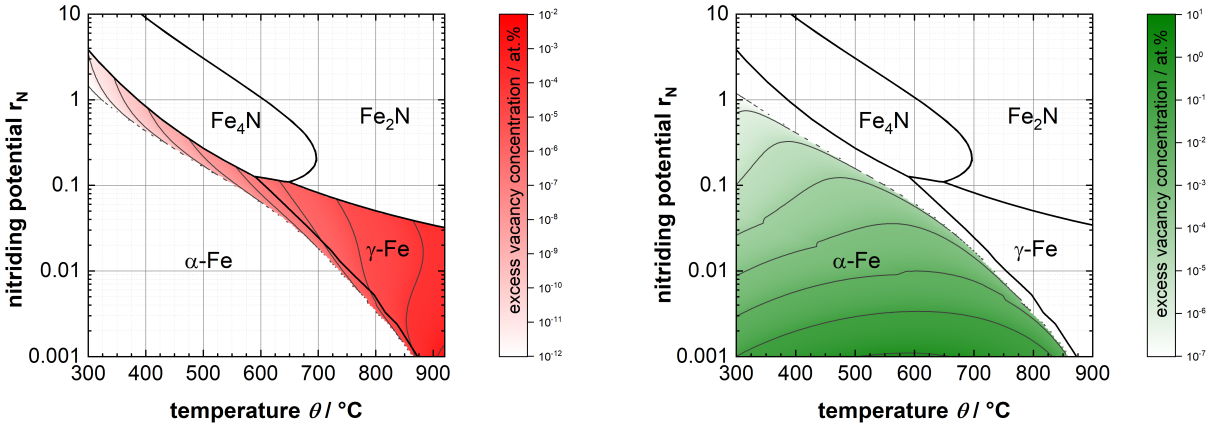

Figure 5: The concentration of excess lone vacancies required in nitrogen-containing α (red contours) and γ (green contours) iron, to shift the phase boundary and expand their respective phase within the Lehrer diagram. The edges of the contour surfaces (where they meet) represent the α-γ phase boundary for a theoretical ideal crystal, so they almost correspond (see figure 4) to the experimentally derived values for this boundary. This study is limited to the α and γ phase boundary. The experimental data (Black lines) is sourced from the FSstel database accessed via FactSage [32] and includes the ϵ (Fe_2N) and γ' (Fe_4N) regions to portray the results of this work in the wider context. Note that the colorbars between both graphs have different ranges of vacancy concentrations.

crystal can provide a moderately precise approximation to experimentally obtained values, and the remaining discrepancies may be reduced further with more resource-heavy DFT computations. Indeed, the experimental boundary lies narrowly within the uncertainty range expected from DFT calculations. If uncertainty ranges were reduced further it would make the distinction between vacancy effects and DFT uncertainty clear.

4. Conclusion

Multiscale modelling was applied to calculate the thermodynamic properties nitrogen in non-ideal iron lattices. This allows advancements towards bridging the gap between simulations at first principles and industrial applications. The α-γ phase boundary in the iron-nitrogen system was assessed from first principles and appears to complement current experimental observations. The phase boundary and nitrogen solubility have been quantified with an explicit dependence on vacancy concentration at conditions which are relevant to nitriding. This improves existing thermodynamic predictions towards vacancy-rich crystals in an applied context. Residual uncertainty from the DFT calculations in this work are carefully quantified, and error bounds for calculated thermodynamic quantities are set using the data uncertainty. Although DFT calculations are well converged relative to current literature, due to limitations of computing resources, the total uncertainties could not always be reduced to the same level from experimental data, particularly with respect to nitrogen-vacancy complex energies. Higher precision would result in even more required computing resources. Despite this, it was determined that there is a credible case that vacancy-rich crystals are in fact more true to reality (than idealised lattices) for the thermodynamic quantities studied. The following conclusions support this case and give cause for further investigation.

- It is a consistent finding in this work and other literature, that vacancy formation energies of the α and γ phases are significantly underestimated in DFT-calculations, compared to experimentally derived values. This indicates that real alloys have far higher (excess) vacancy concentrations than predicted from idealised lattices.

- Nitrogen solubility is underestimated by considering idealised lattices in both phases, and these underestimations lie well outside of the expected uncertainty ranges for the calculations. It is detected following a sensitivity analysis that this is more likely to be due the effect of vacancies (and other crystal imperfections) rather than modelling artifacts. This is supported by experimental nitrogen solubility data, which suggest a large excess

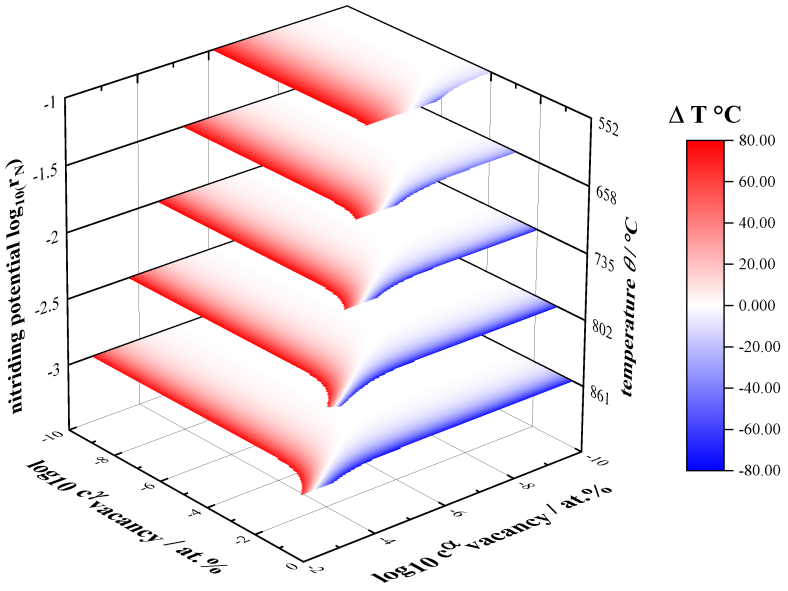

Figure 6: The change of the α-γ phase transition temperature (ΔT) in the presence of nitrogen and excess vacancy concentration on both phases. Each surface represents an evenly spaced (with respect to $\log_{10} r_N$) point on the phase boundary which is calculated for ideal crystals (see figure 4), which are denoted on the vertical axes. The shift is made hotter ($\Delta T > 0\ ^\circ C$) by excess vacancies in α-Fe and colder ($\Delta T < 0\ ^\circ C$) for γ vacancies accordingly. For $\Delta T < -80\ ^\circ C$ or $\Delta T > 80\ ^\circ C$ the surface is left uncoloured for better visibility. Note that the x and y axes depict different ranges of vacancy concentration.

of vacancies to be present in real alloys, even for low nitrogen activities. This deviation may be the result of excess nitrogen at grain boundaries or other crystal imperfections.

- The experimentally derived temperature shift for the α-γ phase boundary (see figure 4) as a function of nitrogen activity is consistently underestimated in the absence of vacancies (i.e. assuming ideal lattices). Whilst the discrepancy between experimental and calculated phase transition temperatures is small and within the range of the predicted calculation uncertainty, the influence of vacancies is more pronounced in the Ferrite (α iron) phase. As shown in figures 5 and 6, small concentrations of additional vacancies in Ferrite can have large effects on the phase transition temperatures, especially at lower temperatures and high nitriding potentials. This is a sign that excess vacancies could be responsible for the discrepancy between calculated and experimental phase boundaries seen in figure 4.

5. Acknowledgements

The authors thank the Centre for Scientific Computing (CSC, University of Warwick) for their support in kindly providing the computation time on their high performance computing cluster.

Appendix A. Calculating $E^{\text{gas}}_{\text{N}_2}$

Total energy calculations of lone nitrogen molecules with an equilibrium bond length of 1.102 Å are performed within a 10×10×10 Å bounding box, at cutoff energies from 500 up to 900 eV using a 12×12×12 k-point grid. When used within the thermodynamic model (see equation 13) the cutoff energy should match that which is used to calculate internal energies, and in table 4 this is 900 eV, which renders the value of very insensitive to further cutoff energy increases. Vibrational frequencies are calculated (at a 900 eV cutoff only) in order to obtain the temperature

dependence of E_2^{gas} in the ideal gas approximation using the formalism provided by the ASE software package, and the software is well documented so details of this are omitted. Using calculated vibrational frequencies, the value of the zero point energy (around 0.146 eV) obtained is in very good agreement with experimental data [33]. The calculated Gibbs Free Energy is also in strong agreement with the experimentally-obtained fit [34] over the temperature range considered in this work, with a maximal discrepancy of no more than ±2 kJ mol^{-1}.

Appendix B. Jump rates used for Kinetic Monte Carlo

Table B.6: Energy barriers (kJ mol^{-1}) for the transition between octahedral positions (ordered by distance to a vacancy) for nitrogen in iron at absolute zero temperature. ∞ positions are deemed far enough from a vacancy that it no longer influences energy barriers.

		Destination			
Start		o_1	o_2	o_3	o_∞
α/δ-Fe	o_1	-	103.3	-	-
	o_2	33.0	-	72.5	-
	o_3	-	48.0	-	74.50
	o_∞	-	-	70.29	70.29
γ-Fe	o_1	-	252.7	-	-
	o_2	192.1	218.2	-	218.2
	o_∞	-	218.2	-	218.2

References

[1] M. Somers, R. Lankreijer, E. Mittemeijer, Excess nitrogen in the ferrite matrix of nitrided binary iron-based alloys, Philosophical Magazine A 59 (2006) 353–378 (2006).

[2] J. Slycke, E. Mittemeijer, M. Somers, 1 - thermodynamics and kinetics of gas and gas-solid reactions, in: Thermochemical Surface Engineering of Steels, 1st Edition, Woodhead Publishing, Oxford, 2015, pp. 3 – 111 (2015). doi:https://doi.org/10.1533/9780857096524.1.3.

[3] M. Auinger, M. Rohwerder, Coupling diffusion and thermodynamics - exemplified for the gas nitriding of iron-chromium alloys, HTM Journal of Heat Treatment and Materials 66 (2011) 100–102 (2011).

[4] B. Kooi, M. Somers, E. Mittemeijer, An evaluation the fe-n phase diagram of considering long-range order of n atoms in $\gamma' - fe_4n1 - x$ and ϵ-fe$_2$n$_{1-z}$, Metallurgical and Materials Transactions A 27A (4) (1996) 1063–1071 (1996).

[5] H. Du, A reevaluation of the fe-n and fe-c-n systems, Journal of Phase Equilibria 14 (6) (1993) 682–693 (1993).

[6] K. Frisk, A new assessment of the fe-n phase diagram, CALPHAD 11 (2) (1987) 127–134 (1987).

[7] F. Bottoli, G. Winther, T. Christiansen, K. Dahl, M. Somers, Low-temperature nitriding of deformed austenitic stainless steels with various nitrogen contents obtained by prior high-temperature solution nitriding, Metallurgical and Materials Transactions A 47 (2016) 4146–4158 (2016).

[8] M. Auinger, E. Müller-Lorenz, M. Rohwerder, Modelling and experiment of selective oxidation and nitridation of binary model alloys at 700°c - the systems fe, 1wt.%{Al, Cr, Mn, Si}, Corrosion Science 90 (2015) 503–510 (2015).

[9] C. Barouh, T. Schuler, C. Fu, M. Nastar, Interaction between vacancies and interstitial solutes (c, n, and o) in α-fe: From electronic structure to thermodynamics, Physical Review B 90 (2014) 054112 (2014).

[10] S. Sakuraya, K. Takahashi, N. Hashimoto, S. Ohnuki, The effect of point defects on diffusion pathway within α-fe, Journal of Physics Condensed Matter 27 (2015) 175007 (2015).

[11] M. Wu, X. Liu, J. Gu, Z. Jin, Dft study of nitrogen-vacancy complexions in (fcc) fe, Modelling and Simulation in Materials Science and Engineering 22 (2014) 055004 (2014).

[12] F. Ye, K. Tong, Y. Wang, Z. Li, F. Zhou, First-principles study of interaction between vacancies and nitrogen atoms in fcc iron, Computational Materials Science 149 (2018) 65–72 (2018).

[13] J. Mortensen, L. Hansen, K. Jacobsen, Real-space grid implementation of the projector augmented wave method, Phys. Rev. B 71 (2005) 035109 (2005).

[14] J. Enkovaara, C. Rostgaard, J. Mortensen, J. Chen, M. Dułak, L. Ferrighi, J. Gavnholt, C. Glinsvad, V. Haikola, H. Hansen, H. Kristoffersen, M. Kuisma, A. Larsen, L. Lehtovaara, M. Ljungberg, O. Lopez-Acevedo, P. Moses, J. Ojanen, T. Olsen, V. Petzold, N. Romero, J. Stausholm-Müller, M. Strange, G. Tritsaris, M. Vanin, M. Walter, B. Hammer, H. Häkkinen, G. Madsen, R. Nieminen, J. Nørskov, M. Puska, T. Rantala, J. Schøtz, K. Thygesen, K. Jacobsen, Electronic structure calculations with gpaw: a real-space implementation of the projector augmented-wave method, Journal of Physics: Condensed Matter 22 (2010) 253202 (2010).

[15] J. Perdew, K. Burke, M. Ernzerhof, Generalized gradient approximation made simple, Phys. Rev. Lett. 77 (1996) 3865–3868 (1996).

[16] A. Larsen, J. Mortensen, J. Blomqvist, I. Castelli, R. Christensen, M. Du/*l*ak, J. Friis, M. Groves, B. Hammer, C. Hargus, E. Hermes, P. Jennings, P. Jensen, J. Kermode, J. Kitchin, E. Kolsbjerg, J. Kubal, K. Kaasbjerg, S. Lysgaard, J. Maronsson, T. Maxson, T. Olsen, L. Pastewka, A. Peterson, C. Rostgaard, J. Schiøtz, O. Schütt, M. Strange, K. Thygesen, T. Vegge, L. Vilhelmsen, M. Walter, Z. Zeng,

K. Jacobsen, The atomic simulation environment - a python library for working with atoms, Journal of Physics: Condensed Matter 29 (2017) 273002 (2017).
[17] H. Monkhorst, J. Pack, Special points for brillouin-zone integrations, Phys. Rev. B 13 (1976) 5188–5192 (1976).
[18] M. Methfessel, A. Paxton, High-precision sampling for brillouin-zone integration in metals, Phys. Rev. B 40 (1989) 3616–3621 (1989).
[19] H. Jónsson, G. Mills, K. Jacobsen, Nudged elastic band method for finding minimum energy paths of transitions, pp. 385–404.
[20] G. Henkelman, B. Uberuaga, H. Jónsson, A climbing image nudged elastic band method for finding saddle points and minimum energy paths, The Journal of Chemical Physics 113 (22) (2000) 9901–9904 (2000).
[21] E. Bitzek, P. Koskinen, F. Gähler, M. Moseler, P. Gumbsch, Structural relaxation made simple, Phys. Rev. Lett. 97 (2006) 170201 (2006).
[22] A. Dinsdale, Sgte data for pure elements, Calphad 15 (4) (1991) 317–425 (1991).
[23] M. Wu, X. Liu, J. Gu, Z. Jin, First-principles simulations of iron with nitrogen: from surface adsorption to bulk diffusion, Modelling and Simulation in Materials Science and Engineering 21 (4) (2013) 045004 (2013).
[24] R. Nazarov, T. Hickel, J. Neugebauer, First-principles study of the thermodynamics of hydrogen-vacancy interaction in fcc iron, Physical Review B 82 (2010) 224104 (2010).
[25] H. Wriedt, N. Gokcen, R. Nafziger, The fe-n (iron-nitrogen) system, Bulletin of Alloy Phase Diagrams 8 (4) (1987) 355–377 (1987).
[26] S. Waele, K. Lejaeghere, E. Leunis, L. Duprez, S. Cottenier, A first-principles reassessment of the fe-n phase diagram in the low-nitrogen limit, Journal of Alloys and Compounds 775 (2019) 758–768 (2019).
[27] S. Kim, W. Buyers, Vacancy formation energy in iron by positron annihilation, Journal of Physics F: Metal Physics 8 (5) (1978) L103–L108 (1978).
[28] T. Schuler, M. Nastar, F. Soisson, Vacancy-induced dissolution of precipitates in out-of-equilibrium systems: A test case of fe x (x = c ,n,o) alloys, Physical Review B 95 (2017) 014113 (2017).
[29] T. Schuler, C. Barouh, M. Nastar, C. Fu, Equilibrium vacancy concentration driven by undetectable impurities, Physical review letters 115 (2015) 015501 (2015).
[30] C. Forst, J. Slycke, K. Vliet, S. Yip, Point defect concentrations in metastable fe-c alloys, Phys. Rev. Lett. 96 (2006) 175501 (2006).
[31] Z. You, M. Paek, I. Jung, Critical evaluation and optimization of the fe-n, mn-n and fe-mn-n systems, Journal of Phase Equilibria and Diffusion 39 (5) (2018) 650–677 (2018).
[32] C. Bale, E. Bélisle, P. Chartrand, S. Decterov, G. Eriksson, K. Hack, I. Jung, Y. Kang, J. Melancon, A. Pelton, C. Robelin, S. Petersen, Factsage thermochemical software and databases - recent developments, CALPHAD 33 (2009) 295–311 (2009).
[33] K. Irikura, Experimental vibrational zero-point energies: Diatomic molecules, Journal of Physical and Chemical Reference Data 36 (2007) 389–397 (2007).
[34] M. Chas, NIST-JANAF thermochemical tables, 4th Edition, American Institute of Physics for the National Institute of Standards and Technology, 1998 (1998).

Thermodynamics of the iron-nitrogen system with vacancies. From first principles to applications

Aurash Karimi[a,*], Michael AUINGER[a,*]

[a]*WMG, University of Warwick, Coventry CV4 7AL, United Kingdom*

Abstract

Density Functional Theory (DFT) and Atomistic Kinetic Monte Carlo is employed in this work to assess the thermodynamic behaviour of the α (BCC) and γ (FCC) allotropes in the iron-nitrogen system. The calculated nitrogen solubility at unit nitrogen activity from ($250 < T < 1538\ ^{\circ}C$) is found to be significantly underestimated, beyond the uncertainty range of the calculation, in both phases. The boundary of the α-γ phase change as featured in Lehrer diagrams is calculated within the nitriding potential ($0.001 < r_N < 10$) and temperature ($300 < T < 900\ ^{\circ}C$) ranges. The boundary shows good agreement with experimental data, but the calculated α region is consistently smaller than the data suggests. Motivated by the existence of grain boundaries and other common defects which cause far more unoccupied volume within iron than is expected in idealised lattice structures, the effect of excess vacancy concentrations in varying ranges between $10^{-12} < c_v < 10$ at.% on nitrogen solubility and the α-γ phase change is quantified. It is shown how discrepancies between the theoretical ideal crystal and experimental data can be "corrected" by excess vacancies to model the non-ideality of iron lattices in reality, and evidence is given for the validity of this correction. Results are presented in an applied context, allowing opportunities for experimental verification.

Keywords:
A. metals and alloys, B. solid state reactions, C. atomic scale structure, C. phase transitions, C. point defects, D. thermodynamic modelling

1. Introduction

Nitriding is an important process to increase mechanical strength and wear resistance of metallic work pieces such as cutting blades, gearwheels and crankshafts. By creating an atmosphere with high nitrogen activity, conventional nitriding processes such as gas nitriding and plasma nitriding lead to the formation of a hard surface layer (termed *compound layer*) that is composed of ϵ and γ'-type iron nitrides. A *diffusion layer* which may comprise of nitrides, both in the α and γ matrix is formed underneath the compound layer [1, 2, 3].
Isolated iron which perfectly conforms to a body centered (α-Fe) or face centered (γ-Fe) cubic lattice arrangement does not exist in reality; numerous imperfections in the crystal structure may be observed, even in alloy grades which are processed specifically to maximise purity. In experimental determination of thermodynamic properties (of the iron-nitrogen system [4, 5, 6]), this fact is usually not considered, as high purity samples are generally considered good approximations of perfect purity. However, the difference in thermodynamic behaviour between (theoretical) ideal, high purity and more significantly deformed; subjugated to irradiation, ball-milling or shot-peening for instance; crystal structures is currently uncertain.
Common defects in industrial iron alloy grades, such as grain boundaries, reduce the packing efficiency of iron atoms which means there is excess unoccupied volume within the structure [7]. Due to this, iron alloys in nature may behave as if they are far more vacancy-rich than simulated idealised lattices under the same conditions [8]. Thus, this work explores the case where the concentration of lone vacancies is held fixed out of equilibrium to be far more plentiful.

*Corresponding authors
Email addresses: a.karimi@warwick.ac.uk (Aurash Karimi), m.auinger@warwick.ac.uk (Michael AUINGER)

An otherwise-ideal iron lattice is considered from first principles using Density Functional Theory (DFT) which contains lone nitrogen interstitials, vacancies and nitrogen-(mono)vacancy complexes, as these point defects carry large significance but are relatively simple. It is quite apparent from recent DFT studies that for both α [9, 10] and γ [11, 12] iron phases that octahedral sites in the proximity of vacancies act as trapping sites for nitrogen, which leads to the formation of complexes at thermal equilibrium in quantities far beyond that of lone vacancies. However, current literature lacks quantified evaluations on the potential thermodynamic influences from nitrogen-vacancy complexes in an explicitly applied context, motivating the work that follows.
In this work a thermodynamic model (section 2.2) is used to reassess the solubility and phase stability with an explicit dependence on excess vacancies for the α and γ phases. DFT assessments of the defects considered, which the thermodynamic model depends on, are outlined in section 2.1, which entails the calculation of both internal energy of individual defects and energy barriers of nitrogen diffusion. Preceding this, the methods section opens with a high-level summary of the theoretical considerations in this work, and the notation used throughout.

2. Methods

Model Description and Notation. The nitriding process is modelled by assuming that there is abundant nitrogen at the surface of an iron alloy (due to the high activity of nitrogen) which proceeds into the material via interstitial diffusion [8, 3]. Dissolved nitrogen may then interact with lone vacancies (denoted v) or nitrogen-vacancy complexes (denoted vN_j) where j is the number of nitrogen atoms within the complex. The process is governed by elementary reactions 1 and 2.

$$\frac{1}{2}\,\mathrm{N}_2 \quad \rightleftharpoons \quad [\mathrm{N}] \tag{1}$$

$$[\mathrm{N}] + [\mathrm{vN}_{j-1}] \quad \rightleftharpoons \quad [\mathrm{vN}_j] \tag{2}$$

Let i denote chemical components of reaction 1 or 2 and $s \in \{\mathrm{gas}, \alpha, \gamma\}$ be the state of i, which are diatomic gas, or interstitially dissolved within octahedral sites in either an α or γ phase Fe lattice respectively. $E_i^s(T)$ and c_i^s denote the internal energy and concentration of i in state s respectively. At absolute zero the internal energy E_i^s is defined as $E_i^s(0)$. At thermodynamic equilibrium with fixed temperature and pressure the concentrations are $c_i^{s_{eq}}$.
The rate at which nitrogen enters the proximity of a vacancy from the atmosphere, denoted $r^s_{\mathrm{enter}}(T)$, is the forward rate at which reaction (1 & 2) proceeds. The rate-determining step of this reaction is assumed to be the interstitial diffusion of nitrogen to reach a vacancy, which is the forward reaction of 2, hence $r^s_{\mathrm{enter}}(T)$ is considered to be approximately equal to the forward rate of 1. The opposing rate at which nitrogen leaves the proximity of a vacancy, denoted $r^s_{\mathrm{leave}_j}(T)$, is then a backward rate of reaction 2. Collectively, these rates define the distribution of nitrogen between complex sites, lone nitrogen defects and the gas state at a given temperature. $R = 8.314$ J mol^{-1} K^{-1} is the universal gas constant which is used throughout this work.

2.1. Atomic Scale Modelling

DFT calculations were carried out with the projector augmented wave method as implemented in GPAW [13, 14]. The Perdew, Burke and Ernzerhof (PBE) exchange-correlation functional [15] was used in all plane wave calculations. The atomic software library ASE [16] was used to interface with GPAW. Ferromagnetic (FM) body centered cubic (BCC) Fe and non-magnetic (NM) face centered cubic (FCC) Fe supercells are used as samples of α and γ phase Fe respectively. A full breakdown of parameters used in DFT calculations is given in tables 1 & 2.

The parameters which are chosen for each DFT calculation are the kinetic cut-off energy for plane-wave functions E_{cut}, the number of k-points distributed in the Brillouin zone using the Monkhurst-Pack method [17], the supercell size, and Methfessel-Paxton [18] (first order) smearing. The smearing width is set to 0.1 for all calculations. For non-smearing parameters, an estimate for the maximum residual uncertainty in output energy with respect to each parameter is considered. E_{cut} and k-points are increased until there is < 0.02 eV residual uncertainty for each supercell size considered. Convergence with respect to supercell size requires case-specific treatment as it is the most sensitive trade-off of computational burden against accuracy. (see closing paragraph of sections 2.1.1 and 2.1.2).

Table 1: Parameter sets for the plane wave DFT calculations used in calculation of internal energies. Error and cut off energy values are given in eV. For temperature-dependent values, u is the maximum uncertainty over the largest temperature range used. u values of - are not explicitly calculated but are inferred to be small with respect to total error.

Energy	E_{cut}	u	supercell	u	kpts	u	u_{total}
E^{α}_{N}	900	0.003	4×4×4	0.013	4×4×4	0.014	0.030
$E^{\alpha}_{\text{N}}(T)$		-	3×3×3	0.037 + 0.003	8×8×8	-	0.040
E^{α}_{v}		< 0.001		0.004		< 0.001	0.004
$E^{\alpha}_{\text{vN}_j}$		0.003		0.055		0.008	0.066
$E^{\alpha}_{\text{vN}_j}(T)$		-		0.037 + 0.019		-	0.056
E^{γ}_{N}		0.003		0.018	12×12×12	0.001	0.022
$E^{\gamma}_{\text{N}}(T)$		-		0.023 + 0.003	6×6×6	-	0.026
$E^{\gamma}_{\downarrow}$		< 0.001		0.005		0.009	0.014
$E^{\gamma}_{\text{vN}_j}$		0.003		0.113	12×12×12	0.001	0.117
$E^{\gamma}_{\text{vN}_j}(T)$		-		0.023 + 0.030	6×6×6	-	0.053

Table 2: Parameter sets for the plane wave DFT calculations used in Nudged Elastic Band (NEB) calculations. The remaining uncertainty u in the resulting energy barriers for nitrogen jumps in iron lattices found for each parameter are given in eV. A u value of - is not explicitly known but inferred to be small with respect to total error. E^{s}_{∞} and $E^{\alpha}_{x\to y}$ denote vacancy-free and vacancy-containing supercells in the NEB respectively.

Energy	E_{cut}	u	supercell	u	kpts	u	u_{total}
$E^{\alpha}_{x\to y}$	500	< 0.001	3×3×3	0.009	8×8×8	-	0.010
E^{γ}_{∞}		< 0.001	2×2×2	< 0.001	8×8×8	-	0.001
$E^{\gamma}_{x\to y}$		< 0.001	3×2×2	0.035	6×8×8	-	0.036

2.1.1. Internal Energies

Calculating $E^{s}_{i}(T)$. Let $\tilde{E}(\text{Fe}_n X)$ be the relaxed energy of a DFT supercell with n iron atoms and crystal structure s. Internal energies E^{s}_{i}, which can be considered to correspond to infinitely dilute point defects within the supercell approximation, are calculated using equations 3 to 5:

$$E^{s}_{\text{N}} = \tilde{E}(\text{Fe}^{s}_{n}\text{N}) - \tilde{E}(\text{Fe}^{s}_{n}) \tag{3}$$

$$E^{s}_{\text{v}} = \tilde{E}(\text{Fe}^{s}_{n-1}\text{v}) - \frac{n-1}{n}\tilde{E}(\text{Fe}^{s}_{n}) \tag{4}$$

$$E^{s}_{\text{vN}_j} = \tilde{E}(\text{Fe}^{s}_{n-1}\text{vN}_j) - \tilde{E}(\text{Fe}^{s}_{n-1}\text{vN}_{j-1}) \tag{5}$$

When X is a complex, the energy is dependant on location of the nitrogen atoms relative to the vacancy. In this case, E^{s}_{i} is set to the minimal energy found out of all candidate structures of X tested. The value of $E^{s}_{\text{vN}_j} - E^{s}_{\text{N}}$ gives the reaction enthalpy of reaction 2, which indicates the attractiveness of a complex containing j nitrogen atoms to a lone nitrogen defect. If the reaction enthalpy is large and positive then it is not energetically beneficial for nitrogen to migrate to form that size of vacancy. It is assumed in this work that generally, $E^{s}_{\text{vN}_j} - E^{s}_{\text{N}}$ increases with j for $j > 2$ (following assessments from literature [12, 9]). Based on this assumption the inequality

$$2 < n^{\max_s}_{\text{N}} = j \text{ is the largest integer such that: } E^{s}_{\text{vN}_j} - E^{s}_{\text{N}} < 0.5 \text{ eV} \tag{6}$$

is used to set integer $n^{\max_s}_{\text{N}}$ such that the maximum sized complex considered in a thermodynamic model still has a significant contribution to total nitrogen concentration relative to lone interstitial nitrogen. Complexes more containing more nitrogen atoms than $n^{\max_s}_{\text{N}}$ then need not be considered.

Temperature dependence and zero point energy of E^{s}_{i} for each i containing nitrogen is assumed to primarily consist of vibrational contributions, where each nitrogen atom is approximated to behave as a three dimensional harmonic oscillator. Vibrational frequencies are calculated within a supercell representing i by making small displacements to each nitrogen atom and using the resulting energies to assemble a Hessian matrix, resulting in a second order approximation of force constants. This method was used as it is implemented in the ASE software library [16].

Convergence. The degree of convergence of equation 3 with respect to (the number of iron atoms) n for both BCC (n = 2, 16, 54, 128) and FCC (n = 4, 32, 108) crystal structures in cubic supercells is observed with two approaches. In the more commonly used (and computationally cheaper) constant volume (CV) approach the lattice parameter is minimised using the smallest possible cubic supercell of iron and this lattice parameter is held fixed for each larger supercell. The constant pressure (CP) approach accounts for changes in supercell volume due to point defects by recalculation of the stable lattice parameter at each supercell size. The CV and CP values are two candidate values which can be equated to E^s_{N}, so the method which results in the smallest energy difference between the two largest considered supercell sizes is chosen as the final result. Furthermore, a quasi-harmonic approach where 4 sets of vibrational frequencies were calculated at 4 different supercell volumes about the energy minimum was used to determine the impact of thermal expansion on internal energies. The convergence behaviour of adding nitrogen to a complex in a supercell is assumed to be similar to adding a lone nitrogen defect to conserve computing resources, so nitrogen-containing supercells in equation 5 are only considered at a single volume. For n smaller than that used to determine the converged E^s_{N}, a more precise definition of equations 3 and 5 may be obtained by fitting convergence data from the CV approach. Namely, an extra term

$$E^s_{\mathrm{repulse}}(n) = a\frac{\log n}{n^3} + b\frac{\log n}{n^2} + c \tag{7}$$

is added to each equation, which outputs an estimate for the energy difference at n between the true internal energy and the converged 'infinitely dilute' supercell energy. In this study $E^s_{\mathrm{repulse}}(n)$ is only calculated for lone nitrogen defects within α or γ (see table 3), otherwise $E^s_{\mathrm{repulse}}(n) = 0$.

Table 3: Parameters for fitting equation 7, where the output energy may either be in eV or kJ mol^{-1}

defect		a		b		c		range
phase	species	eV	kJ mol^{-1}	eV	kJ mol^{-1}	eV	kJ mol^{-1}	
α	N	-27.27	-2631	57.66	5564	-0.002417	-0.2332	2 < n < 128
γ	N	23.82	2298	26.39	2547	-0.006228	-0.6009	4 < n < 108

2.1.2. Rates of Reaction

Energy Barriers. Nudged elastic band (NEB) [19] calculations were used to calculate energy barriers for nitrogen jumps between interstitial sites both with and without a vacancy present in the supercell. In all cases the NEB images are relaxed with the BFGS algorithm as implemented in ASE until the overall forces are less than 0.5 eV, then climbing image NEB [20] is used with the FIRE relaxation algorithm [21] until the forces are less than 0.025 eV. The energy barrier for a transition between adjacent stable octahedral positions is denoted by $E^s_{x\to y}$. Sites for nitrogen are defined by their distance from a vacancy, so that o^s_j is the j^{th} nearest neighbour to a vacancy. In the case of ideal crystals, each jump between sites is identical, so only one barrier $E^s_{\infty\to\infty} := E^s_{\infty}$ needs to be calculated. Close to a vacancy there is far less symmetry between different sites, so at least one barrier should be defined for each j (see figure 1).

Rates. Reaction rates are defined in the form of

$$r^s_{\mathrm{enter\,/\,leave}}(T) = e^{A-\frac{B}{RT}} \tag{8}$$

The jump rate of nitrogen from x to y is defined by the equation

$$r^s_{x\to y}(T) = \upsilon^s_{x\to y} e^{-\frac{E^s_{x\to y}}{RT}} \tag{9}$$

where $\upsilon_{x\to y}$ is the product of vibrational frequencies of nitrogen in the x position divided by the product of vibrational frequencies in the transition state. Due to symmetrical energy barriers in the ideal crystal, A and B values from equation 8 follow immediately from equation 9. For the non ideal case, the rejection-free variant of the Kinetic Monte Carlo (KMC) algorithm is used to generate trajectories which are used to adapt the asymmetrical jump rates (see table B.6) in the proximity of a vacancy so that the net rate at which nitrogen leaves vacancies can be calculated. Nitrogen is evolved in a trajectory within a cubic simulation box which is made to be as small as possible while still

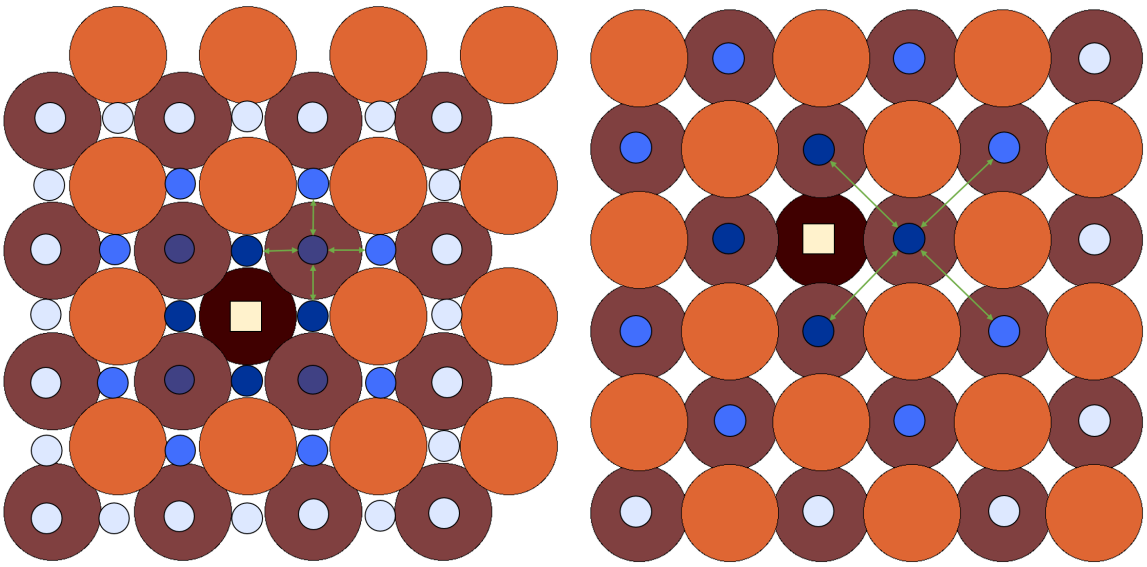

Figure 1: A two-dimensional cross section showing octahedral sites for nitrogen atoms (small circles) within α-Fe (BCC, left) and γ-Fe (FCC, right) lattices of iron atoms (large circles) in the proximity of a vacancy (yellow square). Green arrows represent the jumping directions for nitrogen atoms between sites, which are considered to happen with equal frequency if both ends of the arrow point to the same type of site (shade of blue). The small circles with the darkest shade of blue are the sites which are most influenced by the vacancy, whereas the lightest shade indicates sites which are far enough from the vacancy so that the energy barriers between them are not effected.

containing every type of o_j^s site for which the energy barriers are calculated. The trajectories allow for the calculation of displacement of nitrogen over time at a given temperature. Over a calculated temperature range a linear fit is created from KMC results to calculate A and B.

Convergence. The largest m×m×m or m+1×m×m sized supercells which are possible within computational constraints are used during NEB calculations. In the cuboid supercells, the NEB calculation is oriented so that the largest distance between the initial and ending states are in the periodic $m+1$ direction to minimise symmetry. For a chosen m it is then necessary to decide the maximum number of o_j^s sites which can be considered. Considering more sites provides more energy barriers to calculate rates, but sites which are further away from the vacancy tend to have increased symmetry between periodic images, leading to a decrease in the accuracy of energy barriers. It is immediately clear that j should satisfy $j < \frac{m+1}{2}$, as larger j would result in overlapping site definitions when considering periodicity. It is also ensured that each j satisfies the inequality equation 10.

$$E^s_{j\to(j+1)} - E^s_{j\to(j-1)} > 0 \tag{10}$$

Equation 10 is based on the intuition and previous findings that nitrogen moving towards a vacancy has lower energy barriers than when it is moving away from it. If the inequality is not satisfied, then it would appear that the influence of symmetry is large enough so that E^s_∞ is closer to the true barrier than $E^s_{j\to(j+1)}$, so it is more beneficial to accuracy to treat the site as uninfluenced by the vacancy.

2.2. Thermodynamic Model

Gibbs Free Energy. At fixed temperature T and pressure p, the equation

$$G(T,p) = \sum_{\text{(i, s)}\in\text{reaction}} g(c_i^s, T, p) \tag{11}$$

is defined such that $\frac{\partial g}{\partial c_i^s} = \mu_i^s$, where μ_i^s is the molar chemical potential of i in state s. Thus, the derivative ΔG may represent the Gibbs Free Energy change (of reaction) for reactions 1 and 2. For the purposes of this work, the pressure

dependency of equation 11 in the gas phase can be reduced to just a dependence on the nitrogen partial pressure p_{N_2} with reference pressure $p_0 = 1$ atm [2]. Ammonia is commonly used to create the high nitrogen activity required to dissolve nitrogen in iron in significant quantities. Thus, the partial pressure of nitrogen at fixed temperature can be expressed using the nitriding potential r_N. This is portrayed using the equation

$$p_{N_2} = p_0 \left(r_N e^{13.955 - \frac{6498.0}{T}} \right)^2 \tag{12}$$

which adapts gas equilibrium data for ammonia from [2].

N_2 is treated as a linear ideal gas in order to calculate it's temperature dependent Gibbs Free Energy from first principles using equation

$$g^{\text{gas}}(c_N^{\text{gas}}, T, p_{N_2}) = \frac{1}{2} c_N^{\text{gas}} \left[E_{N_2}^{\text{gas}}(0) - RT \left(S_{\text{other}} + S_{\text{translational}} ln \left(\frac{p_{N_2}}{p_0} \right) \right) \right] \tag{13}$$

The entropy components denoted by S may be calculated from the vibrational frequencies of the nitrogen molecule. Configurational entropy of lone nitrogen defects dissolved within iron is defined by

$$S_{\text{config}}(c, k) = c \; ln \left(\frac{c}{k} \right) + (k - c) \; ln \left(1 - \frac{c}{k} \right) \tag{14}$$

Where c is the ratio of interstitial elements to iron atoms, and k is the number of interstitial positions per iron atom. Equation 14 may be used in a more general definition of configurational entropy for an arbitrary nitrogen and/or vacancy containing defect.

$$S(c_i^s, k) \begin{cases} S_{\text{config}}(c, 1) & n_N^i = 0 \\ S_{\text{config}}(c, k) & n_v^i = 0 \\ S_{\text{config}}(c, 1) - c \; ln \left(n_{\text{permute}}^{n_N^i} \right) & n_v^i = 1, n_N^i > 0 \\ 0 & \text{otherwise} \end{cases} \tag{15}$$

Where n_N^i denotes the number of nitrogen atoms within i, $n_v^i \in \{0, 1\}$ the number of vacancies and $n_{\text{permute}}^{n_N^i}$ is the number of energetically degenerate ways the n_N^i nitrogen atoms may be arranged within the defect. The molar Gibbs Free Energy for a defect with known internal energy (see section 2.1.1) is expressed by

$$g(T, c_i^s) = c_i^s \left(E_i^s(T) + E_{\text{repulse}}^s \left(\frac{1}{c_i^s} \right) \right) + RTS(c_i^s, k) \tag{16}$$

Under the considered range of conditions, the number of defects is not necessarily dilute with respect to the amount of Fe atoms. The significant difference in internal energy caused by repulsion of nitrogen atoms as the concentration increases past around 1 at.% is approximated by the E_{repulse}^s using fitted parameters (for each s) from table 3 (see section 2.1.1 for calculation details).
With equations 13 and 16, g is now defined for each possible i and s combination considered in this work where the defect is present in an arbitrary concentration.

Molar Fractions. If the individual concentrations of each defect considered is known, one may calculate the molar fraction x_x^s of $x \in \{N, v\}$ using the equation

$$x_x^s = \frac{1}{1 + (c_x^{s_{\text{eq}}} + \sum_i^{n_x^i > 0} n_x^i c_i^s)^{-1}} \tag{17}$$

Calculating $c_i^{s_{eq}}$ for each i is equivalent to solving the optimisation problem

$$\min_{c_i^s} G(T, p) \text{ subject to: } c_{N_2}^{\text{gas}} + c_N^{s_{\text{eq}}} = 1 \tag{18}$$

The constraint in equation 18 is physically motivated, with it's purpose to ensure that the concentration of nitrogen available to facilitate reaction 2 is the exactly the amount removed from the atmosphere by reaction 1 per mole of iron

present. Let P_{v}^{s} be defined so that $P_{\mathrm{v}}^{s} c_{\mathrm{v}}^{s_{\mathrm{eq}}}$ is the concentration of vacancies available for reaction 2. Since the formation of the most abundant nitrogen-vacancy complexes is highly favourable if both reactants are in close proximity, it is assumed that the limiting aspect of their formation in the presence of excess vacancies ($P_{\mathrm{v}}^{s} >> 1$) depends on the interstitial diffusion rate of nitrogen. Hence, diffusion (reaction) rates are used to determine equilibrium concentrations of nitrogen-vacancy complexes as opposed to their internal energies. To this end $\hat{c}_{\mathrm{vN}_j}^{s}$ is defined using the mass-action law applied to reaction 2 for successive j (equation 20):

$$\hat{c}_{\mathrm{vN}_j}^{s} = \frac{\left(r_{\mathrm{enter}}^{s}\right)^{j}}{\prod_{m=1}^{m=j} r_{\mathrm{leave}_m}^{s}} \left(c_{\mathrm{N}}^{s}\right)^{j} \tag{19}$$

To investigate the thermodynamic behaviour that occurs when there are excess lone vacancies are present initially, but they aren't readily replenished while the system reaches a (meta)stable state, it should be the case that $\sum_j c_{\mathrm{vN}_j}^{s} \leq P_{\mathrm{v}}^{s} c_{\mathrm{v}}^{s_{\mathrm{eq}}}$. Thus, the equation

$$c_{\mathrm{vN}_j}^{s} = P_{\mathrm{v}}^{s} c_{\mathrm{v}}^{s_{\mathrm{eq}}} \frac{\hat{c}_{\mathrm{vN}_j}^{s}}{\sum_j \hat{c}_{\mathrm{vN}_j}^{s}} \tag{20}$$

is used to obtain the concentration of each nitrogen-vacancy complex.

Phase Change. The thermal stability of nitrogen within the α and γ phases relative to the reference state of nitrogen gas at fixed T and p_{N_2} is defined by

$$F(T, p_{\mathrm{N}_2}, c_{\mathrm{N}}^{s}, c_{\mathrm{v}}^{s}) = g(c_{\mathrm{N}}^{s}, T) + \sum_{j=1}^{n_{\mathrm{N}}^{\max_s}} g(c_{\mathrm{vN}_j}^{s}, T) - g^{\mathrm{gas}}(c_{\mathrm{N}}^{s} + \sum_{j=1}^{n_{\mathrm{N}}^{\max_s}} c_{\mathrm{vN}_j}^{s}, T, p_{\mathrm{N}_2}) \tag{21}$$

Where $n_{\mathrm{N}}^{\max_s}$ corresponds to the maximum number of nitrogen considered for complexes in lattice s. Using equation 21 one may identify one of T, p_{N_2}, P_{v}^{α} or P_{v}^{γ} at which the α-γ phase transition occurs by fixing the other three. For example, to solve for a phase change temperature $\hat{T}$:

- Calculate $c_{\mathrm{N}}^{\alpha_{\mathrm{eq}}}$ and $c_{\mathrm{N}}^{\gamma_{\mathrm{eq}}}$ by applying 18 to the sum of equations 16 and 13
- Let $c_{\mathrm{N}}^{\alpha} = c_{\mathrm{N}}^{\gamma} = max(c_{\mathrm{N}}^{\alpha_{\mathrm{eq}}}, c_{\mathrm{N}}^{\gamma_{\mathrm{eq}}})$
- $\hat{T}$ is a root of the equation

$$F(T, p_{\mathrm{N}_2}, c_{\mathrm{N}}^{\alpha}, c_{\mathrm{v}}^{\alpha}) + \frac{1}{2}[2 - (\mathrm{x}_{\mathrm{v}}^{\alpha} + \mathrm{x}_{\mathrm{v}}^{\gamma})](E_{\mathrm{Fe}}^{\alpha}(T) - E_{\mathrm{Fe}}^{\gamma}(T)) = F(T, p_{\mathrm{N}_2}, c_{\mathrm{N}}^{\gamma}, c_{\mathrm{v}}^{\gamma}) \tag{22}$$

  where $E_{\mathrm{Fe}}^{s}(T)$ is the molar Gibbs Free energy of pure Fe, adapted from [22] in this work.

3. Results and Discussion

3.1. Atomic Scale Results

The lattice parameters for ferromagnetic BCC and non-magnetic FCC iron were found to be 2.838 Å(=0.2838 nm) and 3.461 Å(=0.3461 nm) respectively, with negligible discrepancies for both lattice parameters within previous published DFT literature (see [9, 23] and [24, 11] respectively). In comparison to experimental data [25], the lattice parameter for γ Fe at absolute zero is underestimated by non-magnetic FCC Fe by around 0.11 Å (=0.011 nm), whereas the discrepancy for α Fe is < 0.001 Å (=0.0001 nm). The more significant discrepancy in the γ case is not too surprising, Austenite is known to be both paramagnetic and unstable at absolute zero temperature, both of which are not accounted for in the applied DFT methodology.

3.1.1. Internal Energy

Internal energies at absolute zero temperature calculated in this work are presented in table 4, along with total projected uncertainties with respect to convergence of DFT parameters. A large plane wave cutoff energy E_{cut} value was used in this work relative to other DFT publications (900 eV in this study and 500 ±100 eV in others), which is predicted to correspond to discrepancies of around 0.05 eV (α) and 0.08 eV (γ) in nitrogen-containing defect energies between this work and other literature. There does not currently appear to be a widespread consensus within literature of k-points (relative to supercell size) as in the E_{cut} case, so it is more difficult to predict potential discrepancies in this case. However, halving the number of k-points in each cartesian direction as used in this work amounts to energy differences of at most around 0.1 eV, and the majority of k-point meshes used historically fall within this range. It is common to observe supercell sizes identical to those used in this study or one cubic degree larger (see [26, 12]), so the resulting discrepancies between this work and others due to supercell size should not exceed the uncertainty estimates in table 4. For E^{α}_{N} and E^{γ}_{N}, the uncertainties (± 0.070 eV and 0.048 eV respectively) are relatively insensitive to supercell size. This is because they were calculated using the computationally intensive approach of allowing the lattice parameter to vary at each supercell size. As seen in table 4, the uncertainty for internal energies of nitrogen complexed with vacancies can be several times higher, as they were calculated at fixed lattice parameters and are therefore more sensitive to supercell size. When calculation uncertainty in this work is combined with all the preceding considerations, most literature values fall within the anticipated range of values in this work, which amounts to around ±0.2 eV (= 19.3 kJ mol^{-1}) on average.

Incorporating thermal expansion through the quasi-harmonic approach to calculate the temperature-dependant parts of internal energy was compared to calculating temperature-dependence at the energy minimising volume. Over the 523-1394 K range there were maximum discrepancies of around 0.003 eV per atom for both α and γ. Furthermore, considering three volumes instead of four results in a discrepancy of the same order, so incorporating more volumes when fitting the lattice parameter at each temperature was not considered necessary. The small discrepancy between the single and four-volume cases is due to very minimal lattice expansion found due to the vibrational energy of nitrogen (< 0.001 Å) over the temperature range for both α and γ).

It is noteworthy that in this work and other referenced DFT literature, both E^{α}_{v} = 2.22 eV and E^{γ}_{v} = 2.42 eV are significantly overestimated by their experimental evaluations found with positron annihilation, which are 1.4 ±0.1 eV and 1.7 ±0.2 eV [27] respectively. This supports the earlier prediction of this work, which was that real alloys will have far larger vacancy concentrations than would be expected from idealised iron lattices at thermal equilibrium. Henceforth in this work it is set that $n^{\max_s}_{\text{N}} = 3$, which satisfies equation 6 for both s. Due to the large increase in internal energy from $E^{s}_{\text{vN}_2}$ to $E^{s}_{\text{vN}_3}$ values, earlier assertions that complexes with 2 or less nitrogen atoms tend be to far more abundant than the more nitrogen-rich complexes appear to be true.

3.1.2. Rates of Reaction

The intuition that vacancies tend to trap diffusing nitrogen atoms appears to hold true in both α and γ Fe, with the vacancy having a particularly large effect on the barriers between o^{s}_{1} and o^{s}_{2} sites, causing them to deviate greatly from the ideal crystal activation energy E^{s}_{∞}. The maximum number of sites satisfying equation 10 was found to be 3 for the α phase and 2 for γ using 4x3x3 and 3x2x2 supercells. The difference in the value of $E^{s}_{1\rightarrow2} - E^{s}_{2\rightarrow1}$ between the two largest tested supercells is a good upper bound for uncertainty, as the closest barriers to the vacancy have the largest deviations from E^{s}_{∞} and hence the largest potential for error. The corresponding differences are 0.009 and 0.045 eV for the α and γ phases respectively, so the uncertainty holds some significance in the γ case. It appears that the higher symmetry in the o^{γ}_{2} position for the 2x2x2 cell has caused a high variance in the supercell convergence between different barriers, by underestimating the energy minimum at o^{γ}_{2} and hence widening the energy barrier $E^{\gamma}_{2\rightarrow1}$. Therefore, a moderate increase in accuracy should be achieved in the γ if a larger supercell size can be used within computing constraints. This indicates that while equation 10 is a good overall marker of how many energy barriers can be calculated for a given supercell, it does not necessarily ensure the energy barriers are precise to a level of experimental uncertainty (< 0.01 eV). Between o^{α}_{3} and o^{α}_{4} sites the energy barriers do not deviate largely from E^{α}_{a}, which indicates that at this distance the effect of the vacancy on barriers is largely diminished. Thus, larger supercells to calculate barriers for further positions from the vacancy most likely need not be considered even if computing resources are abundant. In the γ case, using a 2×4×3 supercell which is quite taxing on computing resources still leaves too much symmetry to satisfy equation 10, as $E^{\gamma}_{2\rightarrow3} - E^{\gamma}_{3\rightarrow2}$ = -0.036 eV with this supercell. Employing larger supercells to calculate these barriers may prove beneficial to accuracy, although it is not expected that the energy

Table 4: The calculated Internal energies at zero Kelvin of a singular nitrogen atom or vacancy in various point defects within iron, with corresponding uncertainty estimates and zero-point energies (of nitrogen only). The reference state for each internal energy is that of the full supercell containing the defect, and the tabulated value is the energy which remains (see equations 3-5) when a single nitrogen atom is left. For instance, considering the nitrogen-vacancy complexes, the associated internal energy is of the nitrogen atom which is added to form $E^s_{\mathrm{vN}_j}$ from $E^s_{\mathrm{vN}_{j-1}}$. Identified DFT literature sources are added for comparison, which are adjusted where required using $E^{\mathrm{gas}}_{\mathrm{N}_2}$ in this work so that all values share a common reference state. Abbreviations in parenthesis refer to magnetic states where the magnetism is different to that used in this work.

Defect	Energy		Uncertainty (±)		Zero-point Energy		Literature
	eV	kJ mol^{-1}	eV	kJ mol^{-1}	eV	kJ mol^{-1}	eV
$\frac{1}{2}E^{\mathrm{gas}}_{\mathrm{N}_2}$	-8.450	-815.1	-	-	0.146	14.1	
E^{α}_{N}	-8.198	-791.0	0.070	6.75	0.0982	9.48	-8.13 [28], -8.43[23], -8.317 [26]
E^{α}_{v}	2.22	214.2	0.004	0.39	-	-	2.12 [9]
$E^{\alpha}_{\mathrm{vN}_1}$	-9.080	-876.1	0.112	10.81	0.0894	8.63	-8.91 [9]
$E^{\alpha}_{\mathrm{vN}_2}$	-8.930	-861.6	0.112	10.81	0.0945	9.1	-9.02 [9]
$E^{\alpha}_{\mathrm{vN}_3}$	-7.863	-758.7	0.112	10.81	0.0998	9.63	-7.93 [9]
E^{γ}_{N}	-8.768	-846.0	0.048	4.63	0.128	12.3	-8.609(AFMD) [12]
E^{γ}_{v}	2.42	233.5	0.014	1.35	-	-	2.30 [11] 2.23 [24]
$E^{\gamma}_{\mathrm{vN}_1}$	-9.486	-915.2	0.170	16.40	0.129	12.5	-9.468 [11]
$E^{\gamma}_{\mathrm{vN}_2}$	-9.497	-916.3	0.170	16.40	0.126	12.1	-9.578 [11]
$E^{\gamma}_{\mathrm{vN}_3}$	-8.776	-846.7	0.170	16.40	0.120	11.6	-8.848 [11]

difference in barriers at o^{γ}_3 would be as significant as the difference at o^{α}_3 due to further distance from the vacancy in the γ case. Indeed, the slow supercell convergence is a sign that the true $E^{\gamma}_{2\to3} - E^{\gamma}_{3\to2}$ is relatively small in magnitude, as it is unable to outweigh the effect of symmetry even in relatively large supercells.

Table 5: Reaction rates calculated in this work as defined by equation 8. j indicates the number of nitrogen atoms in the associated complex. * indicates estimated errors deduced from similar calculations

Rate			A	B		Uncertainty (±)	
Direction	phase	j		eV	kJ mol^{-1}	eV	kJ mol^{-1}
enter v	α	-	-5.624	0.727	70.1	0.010	1.0
	γ	-	-4.064	2.247	216.8	0.036	3.5
leave v	α	1	-1.990	1.734	167.3	0.019	1.8
		2	-1.990	1.574	151.9	0.019	1.8*
		3	-1.990	0.528	50.9	0.019	1.8*
	γ	1	-1.583	2.811	271.2	0.045	4.3
		2	-1.583	2.839	273.9	0.045	4.3*
		3	-1.583	2.062	198.9	0.045	4.3*

3.2. Thermodynamic Implications

3.2.1. Solubility

Idealised Iron. The presence of lone nitrogen and vacancies within iron leads to the formation of complexes by reaction 2, and provided there is plentiful nitrogen available at the metal surface, increases the total fractions of nitrogen and vacancies in the system at equilibrium. It is seen from figure 2 that in both iron phases the total fraction of vacancies (equation 17) is heavily dependant on the nitriding potential and temperature, and many orders of magnitude above $c^{s_{\mathrm{eq}}}_{\mathrm{v}}$. This relationship agrees with findings in previous work [29] (α-Fe) and [11] (γ-Fe). The dependence on r_{N} is far stronger in the α case, showing that there is a stronger tendency to form complexes in this phase, which can also be surmised from comparing the internal energies.

The same does not hold for the total fraction of nitrogen, as an insignificant fraction of the nitrogen dissolved within either Fe phase is contained in complexions with vacancies, compared to the amount of lone nitrogen interstitial defects. This is to be expected considering the definition of complex concentrations (equation 20), the product $c^{s_{\mathrm{eq}}}_{\mathrm{v}} c^{s_{\mathrm{eq}}}_{\mathrm{N}}$

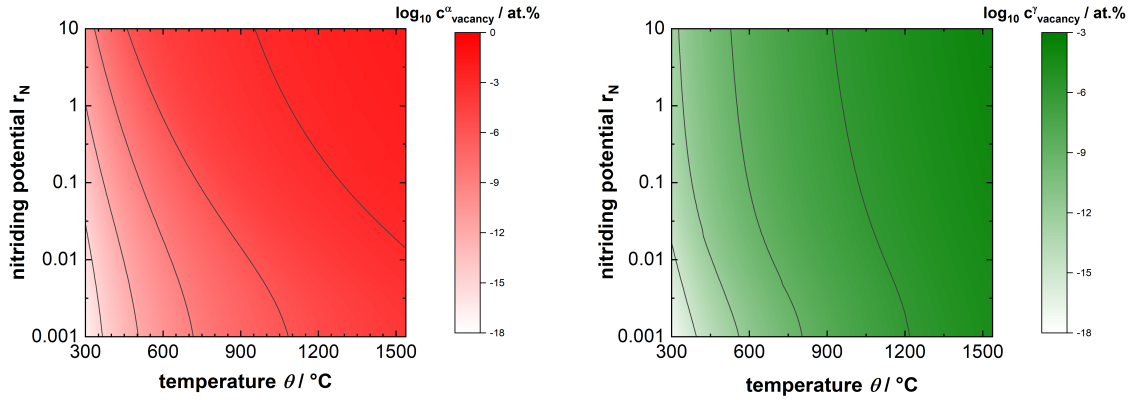

Figure 2: The fraction of vacancies in idealised α (left) and γ (right) iron when nitrogen-vacancy complexes are considered as well as lone vacancies. Note that the upper limit of vacancies reached under these conditions is lower in the γ case and this is reflected in the colour bar axis.

tends to be far smaller than $c_{\mathrm{N}}^{s_{\mathrm{eq}}}$, but relatively close to $c_{\mathrm{v}}^{s_{\mathrm{eq}}}$. Indeed, for hydrogen [24], carbon [30] and previous (γ) nitrogen studies [11] the relationship found between the concentrations of interstitial elements, vacancies (at thermal equilibrium), and their complexes are very similar to the relationship discussed here. The calculated solubility of nitrogen at $p_{\mathrm{N}_2} = 1$ atm up to the melting point of Fe is shown in figure 2 (left). In line with the previous comments, the fraction at equilibrium is almost entirely comprised of lone nitrogen interstitials, meaning that vacancies have little influence on nitrogen solubility at equilibrium. This matches the conclusion from [9] for α-Fe whereas a similar explicit comparison for γ-Fe was not found. In comparison with experimental results (sourced from [25, 31]), there are underestimations in nitrogen solubility beyond the predicted uncertainties in the DFT results of up to an order of magnitude for both phases. If an idealised crystal may indeed be used to calculate the solubility of nitrogen at the same precision of experiments, then the underestimations in $E_{\mathrm{N}}^{s}(T)$ would likely be due to unconsidered temperature-dependant effects. In a sensitivity analysis, a normal distributed error term ($\sim \mathcal{N}(0, 10)$) was added to $E_{\mathrm{N}}^{s}(T)$ (using the lower uncertainty bound energy value at $T = 0$) at evenly spaced intervals over the stable temperature ranges of each phase to create 10000 independent samples. This resulted in 6.84% and 14.5% of the sample solubility's for α and γ respectively exceeding a linear fit of experimental solubility results (on average over the temperature ranges), which corresponds to average over-estimations of internal energies of around 14.9 and 10.5 kJ mol^{-1}. Whilst this magnitude of error is not impossible through systemic DFT errors, phonon energies and magnetic considerations which have not been accounted for in the model, the large and consistent (over both phases) overestimation of energy gives cause to investigate the vacancy-rich case.

Iron with Excess Vacancies. Since vacancies tend to make the dissolution of nitrogen more favourable, the solubility of nitrogen increases when they are in excess. This relationship is depicted in figure 2 (right) for $p_{\mathrm{N}_2} = 1$ atm. It is observed that experimental α solubility values fall within the $0.001 < c_{\mathrm{v}}^{\alpha} < 0.1$ at.% whereas for the γ and δ values $1 < c_{\mathrm{v}}^{\gamma}, c_{\mathrm{v}}^{\delta} < 10$ at.%. However, the uncertainty from DFT calculations remains, as well as the assumptions of the thermodynamic model, so a discrepancy between calculated concentrations vacancy and the true concentrations of an order of a magnitude would not be too surprising. The higher temperature phases appear to contain significantly more vacancies than nitrogen atoms. As the temperature increases, nitrogen is increasingly mobile and has the thermal energy to escape vacancy sites more easily and the trapping effect is weaker. This is observed concretely through the term $\frac{(r_{\mathrm{enter}}^{s})^{j}}{\prod_{m=1}^{m=j} r_{\mathrm{leave}_m}^{s}}$ in equation 20, which tends towards 1 as $T \to \infty$. Particularly at higher temperatures, the expected proportion of excess vacancies appear to make up a substantial proportion of the metal, which may correspond to the large coverage of the interior by grain boundaries and other defects. One may make the general observation that the number of excess vacancies predicted by experimental data in figure 2 is increasing with temperature in each phase. It appears that at lower temperatures nitrogen is less efficient at interacting with vacancies which are suggested to be available at higher temperatures. Finer grain boundaries and stronger vacancy traps could obstruct uniform access to all vacancies for nitrogen at low temperatures, meaning that less vacancies can be "frozen in" to the lattice by nitrogen

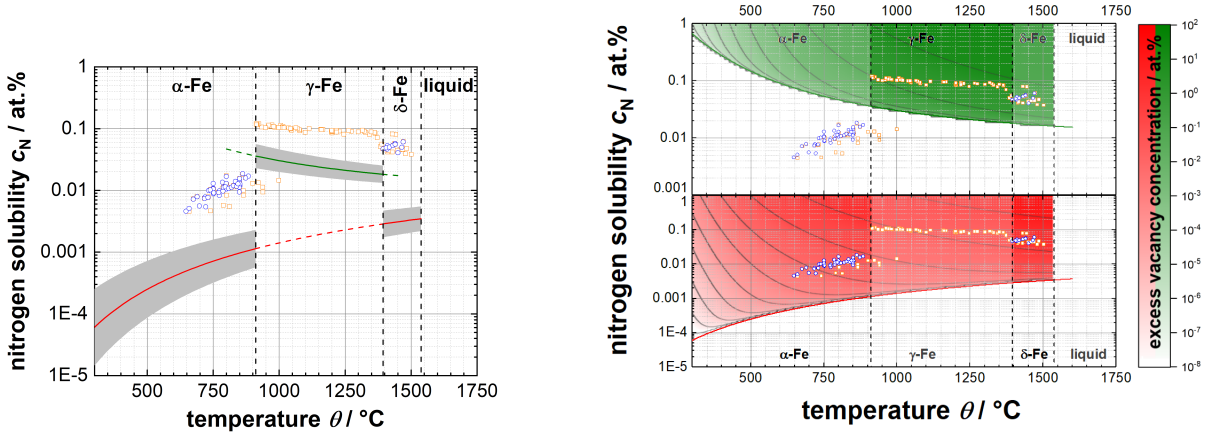

Figure 3: Solubility of nitrogen in iron at nitrogen partial pressure $p_{N_2} = 1$ atm. Experimental values are represented by blue circles [25] and orange circles [31]. In the left image, the solubility of nitrogen in ideal crystals as calculated by DFT is depicted for α (red line) and γ (green line) iron, and DFT calculation uncertainty is represent by the grey shaded area. Excess vacancies, represented by red and green contours, are added to α and γ respectively in right image which increases the solubility of nitrogen above the value obtained from an ideal crystal calculation.

in a given time span. Contrary logic would explain why there is a jump in predicted excess vacancies from the α phase to the γ phase. While diffusion in the γ phase is known to be slower in general, the traps are significantly weaker while the grain boundaries are coarser meaning diffusion directions should be less constrained by vacancies. Indeed, it is assumed that r^s_{enter} is equal the unhindered diffusion rate of nitrogen in the base metal, but in reality imperfections in the crystal structure may inhibit nitrogen atoms from reaching more stable configurations because their access to available vacancies is restricted. At higher temperatures (around 912 $°C$), the variation of excess vacancies with respect to temperature changes reduces sharply, indicating that available vacancies are utilised to a a maximal value. This would explain both the higher variance in the predicted number of vacancies filled, and the increased sparsity of experimental data in the α phase, as less vacancies are required to make relatively large changes to solubility.

3.2.2. Phase Stability

Idealised Iron. As seen in figure 4, the α-γ phase boundary appears to strongly resemble the line obtained from experimental data (FSstel accessed via FactSage [32]). It is not too surprising that the phase boundary is a better fit to experimental data than the calculated nitrogen solubilities at $p_{N_2} = 1$. As the solubility results are underestimated for both phases this leads to consistent changes in energy for both phases in equation 21, so that while absolute energies for each phase may be overestimates of experimental energies, the discrepancy is largely cancelled in the phase boundary computation.

If the $E_{\text{repulse}}(n)$ terms are omitted when calculating the phase boundary, it appears that at lower temperatures and larger r_N the calculated boundary diverges from the experimental data. It seems that the unconstrained internal energy is an under-estimate, so that it results in over-estimations in the value of $c_N^{\gamma_{eq}}$. This is directly linked to supercell convergence, using energy which is not corrected for repulsion in calculating equilibrium concentrations diverges from the true concentration as it increases past the supercell size (i.e for $c_N^{\gamma_{eq}} > \frac{1}{109} \approx 0.0091$) from which the energy originates. The $E_{\text{repulse}}(n)$ terms are extrapolated outside the range prescribed in table 3 to $n = 200$, otherwise a pronounced kink is created in the phase boundary, due to the relatively sudden drop in the derivatives (with respect to r_N and T) of $c_N^{\gamma_{eq}}$. A small kink remains in figure 4 at around 780 $°C$, but it was not deemed necessary to extrapolate to larger n. The thermodynamic model is significantly more (computationally) costly when the repulsion terms are included, and the uncertainty in extrapolation increases with n. It is likely that using information from larger supercells to fit the repulsion energy and expand the range of the repulsion function would result in a smoother (and slightly more accurate) phase boundary if required.

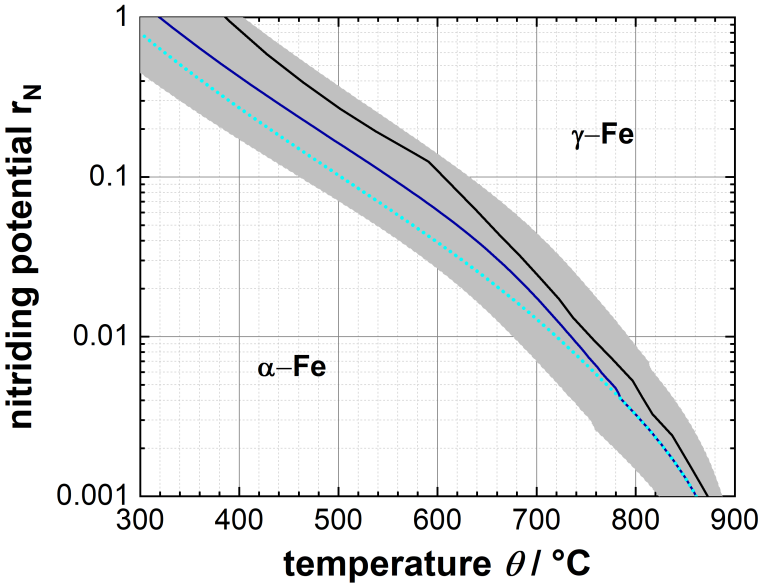

Figure 4: The calculated α-γ phase boundary in the iron-nitrogen system from first principles (blue line) with a corresponding uncertainty range (grey area)). The cyan dots represent the calculated boundary line when the repulsion of dissolved nitrogen atoms is not accounted for in the thermodynamic model. The black line is the corresponding fit of the boundary line from experimental data (sourced from the FSstel database accessed via FactSage [32]). Although in reality there are more stable iron-nitride allotropes in certain regions for the conditions featured, they are not included in this figure for conciseness.

Iron with Excess Vacancies. Since nitrogen-vacancy interactions are energetically favourable, the α-γ phase boundary can become more favoured towards the α-phase or γ-phase (see figure 5) when vacancies are in excess in the respective phases. The thermodynamic model does not take into account the repulsion of nitrogen between complexes, meaning that the total nitrogen fractions within vacancies are expected to be overestimates when a substantial amount of the total nitrogen is contained within them and the total fraction of vacancies is large (> 1 at.%). The attraction of nitrogen-vacancy complexes between each other to form larger complexes, which competes with the repulsion of the contained nitrogen atoms is a relationship which is still under investigation in literature [11, 12, 9], so it is difficult to predict the point at which vacancy complexes will cease to form due to unfavourable repulsion (despite an abundance of vacancies and nitrogen). Nevertheless, the majority of regions in figure 5 (left) should not suffer significant inaccuracies from this, as the regions of the Lehrer diagram with high nitriding potential and temperature tend to contain the largest total fractions of vacancies (see figure 2).

Nitriding conditions commonly have a nitrogen activity which greatly exceeds p_{N_2} = 1 atm, due to abundant nitrogen, nitrogen-vacancy complexes form quickly and most excess vacancies will contain nitrogen when a metastable state is reached. With reference to figure 5, following the contour surface edges to the bottom right from the α-γ-γ' triple point ($r_N = 0.124$, $T = 592°C$), increasingly more vacancies are required to make a noticeable difference to the phase boundaries. As can be seen in figure 6, the surface closest to the triple point is heavily shaded, as a larger range of excess vacancies (with smaller concentrations) may alter the phase change than in the less nitrogen rich surfaces. It is noteworthy that closer to the triple point the phase change is more sensitive to excess vacancies, because the largest deviations from experimental data (see figure 4) are also increasing towards the triple point. Due to higher effectiveness of vacancies as traps in the α case relative to γ, the surfaces in figure 6 are dominated by positive values, meaning that non-ideal of crystals are more likely to favour a larger α phase region. True to this logic, there is consistently an underestimation of the α phase region by the ideal crystal calculation. On the other hand, the temperature difference between the α-γ boundary calculated in this work compared to the experimental data by no more than 80 $°C$ (up to the triple point). It seems that with regards to phase boundary, in contrast to calculations of nitrogen solubility, the ideal

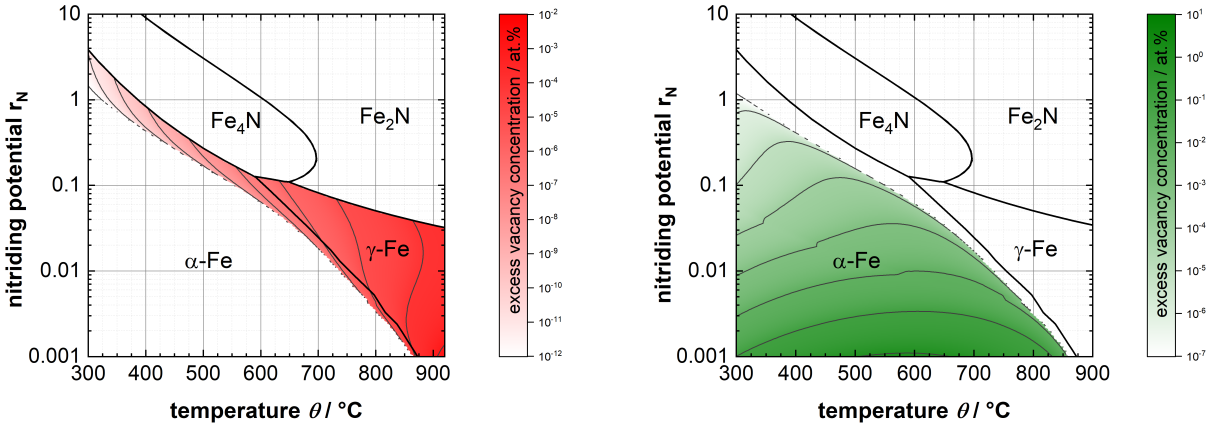

Figure 5: The concentration of excess lone vacancies required in nitrogen-containing α (red contours) and γ (green contours) iron, to shift the phase boundary and expand their respective phase within the Lehrer diagram. The edges of the contour surfaces (where they meet) represent the α-γ phase boundary for a theoretical ideal crystal, so they almost correspond (see figure 4) to the experimentally derived values for this boundary. This study is limited to the α and γ phase boundary. The experimental data (Black lines) is sourced from the FSstel database accessed via FactSage [32] and includes the ϵ (Fe_2N) and γ' (Fe_4N) regions to portray the results of this work in the wider context. Note that the colorbars between both graphs have different ranges of vacancy concentrations.

crystal can provide a moderately precise approximation to experimentally obtained values, and the remaining discrepancies may be reduced further with more resource-heavy DFT computations. Indeed, the experimental boundary lies narrowly within the uncertainty range expected from DFT calculations. If uncertainty ranges were reduced further it would make the distinction between vacancy effects and DFT uncertainty clear.

4. Conclusion

Multiscale modelling was applied to calculate the thermodynamic properties nitrogen in non-ideal iron lattices. This allows advancements towards bridging the gap between simulations at first principles and industrial applications. The α-γ phase boundary in the iron-nitrogen system was assessed from first principles and appears to complement current experimental observations. The phase boundary and nitrogen solubility have been quantified with an explicit dependence on vacancy concentration at conditions which are relevant to nitriding. This improves existing thermodynamic predictions towards vacancy-rich crystals in an applied context. Residual uncertainty from the DFT calculations in this work are carefully quantified, and error bounds for calculated thermodynamic quantities are set using the data uncertainty. Although DFT calculations are well converged relative to current literature, due to limitations of computing resources, the total uncertainties could not always be reduced to the same level from experimental data, particularly with respect to nitrogen-vacancy complex energies. Higher precision would result in even more required computing resources. Despite this, it was determined that there is a credible case that vacancy-rich crystals are in fact more true to reality (than idealised lattices) for the thermodynamic quantities studied. The following conclusions support this case and give cause for further investigation.

- It is a consistent finding in this work and other literature, that vacancy formation energies of the α and γ phases are significantly underestimated in DFT-calculations, compared to experimentally derived values. This indicates that real alloys have far higher (excess) vacancy concentrations than predicted from idealised lattices.

- Nitrogen solubility is underestimated by considering idealised lattices in both phases, and these underestimations lie well outside of the expected uncertainty ranges for the calculations. It is detected following a sensitivity analysis that this is more likely to be due the effect of vacancies (and other crystal imperfections) rather than modelling artifacts. This is supported by experimental nitrogen solubility data, which suggest a large excess

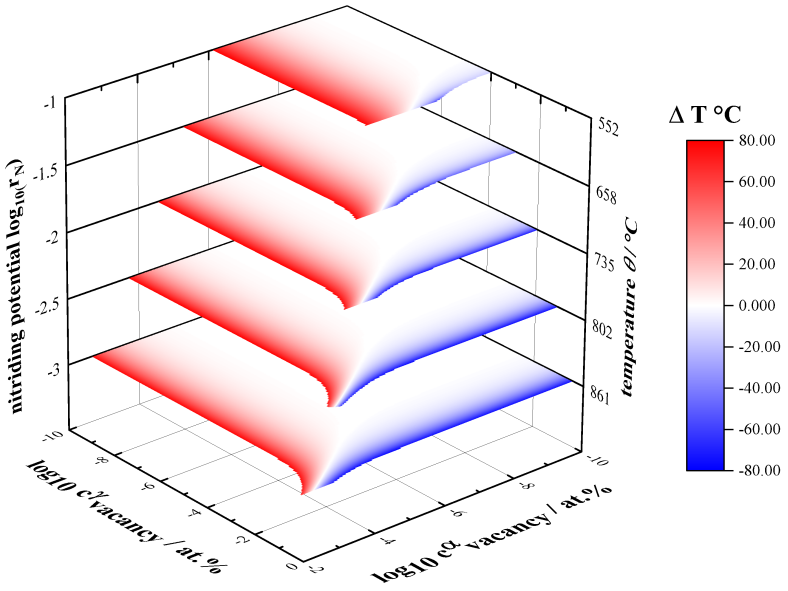

Figure 6: The change of the α-γ phase transition temperature (ΔT) in the presence of nitrogen and excess vacancy concentration on both phases. Each surface represents an evenly spaced (with respect to $\log_{10} r_N$) point on the phase boundary which is calculated for ideal crystals (see figure 4), which are denoted on the vertical axes. The shift is made hotter ($\Delta T > 0\ ^\circ C$) by excess vacancies in α-Fe and colder ($\Delta T < 0\ ^\circ C$) for γ vacancies accordingly. For $\Delta T < -80\ ^\circ C$ or $\Delta T > 80\ ^\circ C$ the surface is left uncoloured for better visibility. Note that the x and y axes depict different ranges of vacancy concentration.

of vacancies to be present in real alloys, even for low nitrogen activities. This deviation may be the result of excess nitrogen at grain boundaries or other crystal imperfections.

- The experimentally derived temperature shift for the α-γ phase boundary (see figure 4) as a function of nitrogen activity is consistently underestimated in the absence of vacancies (i.e. assuming ideal lattices). Whilst the discrepancy between experimental and calculated phase transition temperatures is small and within the range of the predicted calculation uncertainty, the influence of vacancies is more pronounced in the Ferrite (α iron) phase. As shown in figures 5 and 6, small concentrations of additional vacancies in Ferrite can have large effects on the phase transition temperatures, especially at lower temperatures and high nitriding potentials. This is a sign that excess vacancies could be responsible for the discrepancy between calculated and experimental phase boundaries seen in figure 4.

5. Acknowledgements

The authors thank the Centre for Scientific Computing (CSC, University of Warwick) for their support in kindly providing the computation time on their high performance computing cluster.

Appendix A. Calculating $E^{\text{gas}}_{\text{N}_2}$

Total energy calculations of lone nitrogen molecules with an equilibrium bond length of 1.102 Å are performed within a 10×10×10 Å bounding box, at cutoff energies from 500 up to 900 eV using a 12×12×12 k-point grid. When used within the thermodynamic model (see equation 13) the cutoff energy should match that which is used to calculate internal energies, and in table 4 this is 900 eV, which renders the value of very insensitive to further cutoff energy increases. Vibrational frequencies are calculated (at a 900 eV cutoff only) in order to obtain the temperature

dependence of E_2^{gas} in the ideal gas approximation using the formalism provided by the ASE software package, and the software is well documented so details of this are omitted. Using calculated vibrational frequencies, the value of the zero point energy (around 0.146 eV) obtained is in very good agreement with experimental data [33]. The calculated Gibbs Free Energy is also in strong agreement with the experimentally-obtained fit [34] over the temperature range considered in this work, with a maximal discrepancy of no more than ±2 kJ mol^{-1}.

Appendix B. Jump rates used for Kinetic Monte Carlo

Table B.6: Energy barriers (kJ mol^{-1}) for the transition between octahedral positions (ordered by distance to a vacancy) for nitrogen in iron at absolute zero temperature. ∞ positions are deemed far enough from a vacancy that it no longer influences energy barriers.

		Destination			
Start		o_1	o_2	o_3	o_∞
α/δ-Fe	o_1	-	103.3	-	-
	o_2	33.0	-	72.5	-
	o_3	-	48.0	-	74.50
	o_∞	-	-	70.29	70.29
γ-Fe	o_1	-	252.7	-	-
	o_2	192.1	218.2	-	218.2
	o_∞	-	218.2	-	218.2

References

[1] M. Somers, R. Lankreijer, E. Mittemeijer, Excess nitrogen in the ferrite matrix of nitrided binary iron-based alloys, Philosophical Magazine A 59 (2006) 353–378 (2006).

[2] J. Slycke, E. Mittemeijer, M. Somers, 1 - thermodynamics and kinetics of gas and gas-solid reactions, in: Thermochemical Surface Engineering of Steels, 1st Edition, Woodhead Publishing, Oxford, 2015, pp. 3 – 111 (2015). doi:https://doi.org/10.1533/9780857096524.1.3.

[3] M. Auinger, M. Rohwerder, Coupling diffusion and thermodynamics - exemplified for the gas nitriding of iron-chromium alloys, HTM Journal of Heat Treatment and Materials 66 (2011) 100–102 (2011).

[4] B. Kooi, M. Somers, E. Mittemeijer, An evaluation the fe-n phase diagram of considering long-range order of n atoms in $\gamma' - fe_4n1 - x$ and ϵ-fe$_2$n$_{1-z}$, Metallurgical and Materials Transactions A 27A (4) (1996) 1063–1071 (1996).

[5] H. Du, A reevaluation of the fe-n and fe-c-n systems, Journal of Phase Equilibria 14 (6) (1993) 682–693 (1993).

[6] K. Frisk, A new assessment of the fe-n phase diagram, CALPHAD 11 (2) (1987) 127–134 (1987).

[7] F. Bottoli, G. Winther, T. Christiansen, K. Dahl, M. Somers, Low-temperature nitriding of deformed austenitic stainless steels with various nitrogen contents obtained by prior high-temperature solution nitriding, Metallurgical and Materials Transactions A 47 (2016) 4146–4158 (2016).

[8] M. Auinger, E. Müller-Lorenz, M. Rohwerder, Modelling and experiment of selective oxidation and nitridation of binary model alloys at 700°c - the systems fe, 1wt.%{Al, Cr, Mn, Si}, Corrosion Science 90 (2015) 503–510 (2015).

[9] C. Barouh, T. Schuler, C. Fu, M. Nastar, Interaction between vacancies and interstitial solutes (c, n, and o) in α-fe: From electronic structure to thermodynamics, Physical Review B 90 (2014) 054112 (2014).

[10] S. Sakuraya, K. Takahashi, N. Hashimoto, S. Ohnuki, The effect of point defects on diffusion pathway within α-fe, Journal of Physics Condensed Matter 27 (2015) 175007 (2015).

[11] M. Wu, X. Liu, J. Gu, Z. Jin, Dft study of nitrogen-vacancy complexions in (fcc) fe, Modelling and Simulation in Materials Science and Engineering 22 (2014) 055004 (2014).

[12] F. Ye, K. Tong, Y. Wang, Z. Li, F. Zhou, First-principles study of interaction between vacancies and nitrogen atoms in fcc iron, Computational Materials Science 149 (2018) 65–72 (2018).

[13] J. Mortensen, L. Hansen, K. Jacobsen, Real-space grid implementation of the projector augmented wave method, Phys. Rev. B 71 (2005) 035109 (2005).

[14] J. Enkovaara, C. Rostgaard, J. Mortensen, J. Chen, M. Dułak, L. Ferrighi, J. Gavnholt, C. Glinsvad, V. Haikola, H. Hansen, H. Kristoffersen, M. Kuisma, A. Larsen, L. Lehtovaara, M. Ljungberg, O. Lopez-Acevedo, P. Moses, J. Ojanen, T. Olsen, V. Petzold, N. Romero, J. Stausholm-Müller, M. Strange, G. Tritsaris, M. Vanin, M. Walter, B. Hammer, H. Häkkinen, G. Madsen, R. Nieminen, J. Nørskov, M. Puska, T. Rantala, J. Schøtz, K. Thygesen, K. Jacobsen, Electronic structure calculations with gpaw: a real-space implementation of the projector augmented-wave method, Journal of Physics: Condensed Matter 22 (2010) 253202 (2010).

[15] J. Perdew, K. Burke, M. Ernzerhof, Generalized gradient approximation made simple, Phys. Rev. Lett. 77 (1996) 3865–3868 (1996).

[16] A. Larsen, J. Mortensen, J. Blomqvist, I. Castelli, R. Christensen, M. Du/*l*ak, J. Friis, M. Groves, B. Hammer, C. Hargus, E. Hermes, P. Jennings, P. Jensen, J. Kermode, J. Kitchin, E. Kolsbjerg, J. Kubal, K. Kaasbjerg, S. Lysgaard, J. Maronsson, T. Maxson, T. Olsen, L. Pastewka, A. Peterson, C. Rostgaard, J. Schiøtz, O. Schütt, M. Strange, K. Thygesen, T. Vegge, L. Vilhelmsen, M. Walter, Z. Zeng,

K. Jacobsen, The atomic simulation environment - a python library for working with atoms, Journal of Physics: Condensed Matter 29 (2017) 273002 (2017).
[17] H. Monkhorst, J. Pack, Special points for brillouin-zone integrations, Phys. Rev. B 13 (1976) 5188–5192 (1976).
[18] M. Methfessel, A. Paxton, High-precision sampling for brillouin-zone integration in metals, Phys. Rev. B 40 (1989) 3616–3621 (1989).
[19] H. Jónsson, G. Mills, K. Jacobsen, Nudged elastic band method for finding minimum energy paths of transitions, pp. 385–404.
[20] G. Henkelman, B. Uberuaga, H. Jónsson, A climbing image nudged elastic band method for finding saddle points and minimum energy paths, The Journal of Chemical Physics 113 (22) (2000) 9901–9904 (2000).
[21] E. Bitzek, P. Koskinen, F. Gähler, M. Moseler, P. Gumbsch, Structural relaxation made simple, Phys. Rev. Lett. 97 (2006) 170201 (2006).
[22] A. Dinsdale, Sgte data for pure elements, Calphad 15 (4) (1991) 317–425 (1991).
[23] M. Wu, X. Liu, J. Gu, Z. Jin, First-principles simulations of iron with nitrogen: from surface adsorption to bulk diffusion, Modelling and Simulation in Materials Science and Engineering 21 (4) (2013) 045004 (2013).
[24] R. Nazarov, T. Hickel, J. Neugebauer, First-principles study of the thermodynamics of hydrogen-vacancy interaction in fcc iron, Physical Review B 82 (2010) 224104 (2010).
[25] H. Wriedt, N. Gokcen, R. Nafziger, The fe-n (iron-nitrogen) system, Bulletin of Alloy Phase Diagrams 8 (4) (1987) 355–377 (1987).
[26] S. Waele, K. Lejaeghere, E. Leunis, L. Duprez, S. Cottenier, A first-principles reassessment of the fe-n phase diagram in the low-nitrogen limit, Journal of Alloys and Compounds 775 (2019) 758–768 (2019).
[27] S. Kim, W. Buyers, Vacancy formation energy in iron by positron annihilation, Journal of Physics F: Metal Physics 8 (5) (1978) L103–L108 (1978).
[28] T. Schuler, M. Nastar, F. Soisson, Vacancy-induced dissolution of precipitates in out-of-equilibrium systems: A test case of fe x (x = c ,n,o) alloys, Physical Review B 95 (2017) 014113 (2017).
[29] T. Schuler, C. Barouh, M. Nastar, C. Fu, Equilibrium vacancy concentration driven by undetectable impurities, Physical review letters 115 (2015) 015501 (2015).
[30] C. Forst, J. Slycke, K. Vliet, S. Yip, Point defect concentrations in metastable fe-c alloys, Phys. Rev. Lett. 96 (2006) 175501 (2006).
[31] Z. You, M. Paek, I. Jung, Critical evaluation and optimization of the fe-n, mn-n and fe-mn-n systems, Journal of Phase Equilibria and Diffusion 39 (5) (2018) 650–677 (2018).
[32] C. Bale, E. Bélisle, P. Chartrand, S. Decterov, G. Eriksson, K. Hack, I. Jung, Y. Kang, J. Melancon, A. Pelton, C. Robelin, S. Petersen, Factsage thermochemical software and databases - recent developments, CALPHAD 33 (2009) 295–311 (2009).
[33] K. Irikura, Experimental vibrational zero-point energies: Diatomic molecules, Journal of Physical and Chemical Reference Data 36 (2007) 389–397 (2007).
[34] M. Chas, NIST-JANAF thermochemical tables, 4th Edition, American Institute of Physics for the National Institute of Standards and Technology, 1998 (1998).

***Highlights (for review)**

- Idealised Fe structures underestimate nitrogen solubility
- Nitrogen repulsion should be considered within γ-Fe
- Idealised Fe structures underestimate α-Fe stability in nitrogen
- Unexpectedly high vacancy concentrations in Fe
- Vacancies can correct first principles results to match experiments

LaTeX Source Files

Click here to download LaTeX Source Files: Manuscript - Latex source files.zip

*Declaration of Interest Statement

Declaration of interests

☒ The authors declare that they have no known competing financial interests or personal relationships that could have appeared to influence the work reported in this paper.

☐The authors declare the following financial interests/personal relationships which may be considered as potential competing interests: